Exploring the Model Space of Airborne Electromagnetic Data to Delineate Large-Scale Structure and Heterogeneity within an Aquifer System

SEOGI KANG[1], R Knight[1], T Greene[2], C Buck[3], and G Fogg[4]

[1]Stanford University
[2]California State University
[3]Butte County
[4]University of California, Davis

November 24, 2022

Abstract

Airborne electromagnetic (AEM) data can be inverted to recover models of the electrical resistivity of the subsurface; these, in turn, can be transformed to obtain models of sediment type. AEM data were acquired in Butte and Glenn Counties, California, U.S.A. to improve the understanding of the aquifer system. Around 800 line-kilometers of high-quality data were acquired, imaging to a depth of ~300 m. We developed a workflow designed to obtain, from the AEM data, information about the large-scale structure and heterogeneity of the aquifer system to better understand the vertical connectivity. Using six different forms of inversion and posterior sampling of the recovered resistivity models, we produced 6006 resistivity models. These models were transformed to models of sediment type and estimates of percentage of sand/gravel. Exploring the model space, containing the resistivity models and the derived models, allowed us to delineate the large-scale structure of the aquifer system in a way that captures and communicates the uncertainty in the identified sediment type. The uncertainty increased, as expected, with depth, but also served to indicate, as areas of high uncertainty in sediment type, the location of both large-scale and small-scale interfaces between sediment type. A plan view map of the integrated percentage of sand/gravel, when compared to existing hydrographs, revealed the extent of lateral changes in vertical connectivity within the aquifer system throughout the study area.

Exploring the Model Space of Airborne Electromagnetic Data to Delineate Large-Scale Structure and Heterogeneity within an Aquifer System

S. Kang[1], R. Knight[1], T. Greene[2], C. Buck[3], and G. Fogg[4]
[1]Stanford University.
[2]California State University, Chico
[3]Dept. of Water and Resource Conservation, Butte County.
[4]University of California, Davis.

Corresponding author: Seogi Kang (sgkang09@stanford.edu)

Key Points:

- Using multiple forms of inversion, we designed a workflow that can derive many resistivity and sediment-type models from AEM data.
- Models of sediment type reveal the large-scale architecture of the aquifer system
- The estimated uncertainty in sediment type reveals the presence of changes in sediment type.
- Models of the percentage of sand/gravel, when combined with hydrographs, provide useful information about the lateral variability in vertical connectivity within the aquifer system.

Abstract

Airborne electromagnetic (AEM) data can be inverted to recover models of the electrical resistivity of the subsurface; these, in turn, can be transformed to obtain models of sediment type. AEM data were acquired in Butte and Glenn Counties, California, U.S.A. to improve the understanding of the aquifer system. Around 800 line-kilometers of high-quality data were acquired, imaging to a depth of ~300 m. We developed a workflow designed to obtain, from the AEM data, information about the large-scale structure and heterogeneity of the aquifer system to better understand the vertical connectivity. Using six different forms of inversion and posterior sampling of the recovered resistivity models, we produced 6006 resistivity models. These models were transformed to models of sediment type and estimates of percentage of sand/gravel. Exploring the model space, containing the resistivity models and the derived models, allowed us to delineate the large-scale structure of the aquifer system in a way that captures and communicates the uncertainty in the identified sediment type. The uncertainty increased, as expected, with depth, but also served to indicate, as areas of high uncertainty in sediment type, the location of both large-scale and small-scale interfaces between sediment type. A plan view map of the integrated percentage of sand/gravel, when compared to existing hydrographs, revealed the extent of lateral changes in vertical connectivity within the aquifer system throughout the study area.

Plain Language Summary

In studying and managing groundwater systems, it can be very difficult to get the information needed about the subsurface. The airborne electromagnetic (AEM) method uses a helicopter to move a geophysical system over the land surface, acquiring data that can be used to obtain 3D models of the electrical resistivity of the subsurface. In this study we acquired ~800 line-kilometers of high-quality AEM data in an area of Butte and Glenn Counties in the Central Valley of California, U.S.A. Acquisition of these data allowed us to obtain 3D resistivity models covering the region from the ground surface to a depth of about 300 m. Working with descriptions from wells, we were able to transform the 3D resistivity models into 3D sediment-type models. These models allowed us to map out the large-scale structure of the groundwater system and better understand the vertical connectivity within the system. Because of fundamental limitations in the AEM method, we obtained many different resistivity models and corresponding sediment type. Exploring these subsurface models allowed us to quantify the uncertainty in our interpretation of the data. This not only assisted in our interpretation, but it also communicated, to the local water agency, our confidence in our interpretation.

1. Introduction

The airborne electromagnetic (AEM) method can play an important role in the study and management of groundwater systems, by providing a model of the subsurface that captures the large-scale variation in lithology or sediment type throughout a survey area. A typical workflow for the interpretation of AEM data involves the compilation and review of all relevant ancillary data from the survey area (e.g. lithology logs, geophysical logs, geological cross-sections); the initial processing of the acquired data, to remove low quality data; the inversion of the data, to recover the electrical resistivity distribution in the subsurface and define a resistivity model; and the transformation of the electrical resistivity model into a 3D model of lithology or sediment type. The inversion step introduces significant uncertainty into the workflow due to the non-uniqueness in AEM inverse problems. This results in significant uncertainty in the derived 3D model of lithology or sediment type; that is, there are many models of lithology or sediment type that are compatible with the acquired AEM data. It is thus essential, if subsurface models derived from AEM data are to be used as the basis for groundwater science or management, that methods are developed that can account for and quantify the uncertainty.

One well-established concept that accounts for a specific form of uncertainty is the depth-of-investigation (DOI) which has been adopted to refer to the depth below which the recovered resistivity model is presumed to be unreliable due to the decreasing resolution of AEM data with depth (Oldenburg & Li 1999; Vest Christiansen & Auken 2012). Importantly, however, there is uncertainty in the portion of the model above the DOI, inherent to AEM inversion, that will impact this region; i.e. there are many different resistivity models, and therefore lithology or sediment-type models, that can fit the data. Previous work on this topic has addressed the gradient-based (Auken et al., 2015; Viezzoli et al., 2008) and stochastic optimization approaches (Christensen et al., 2017; Minsley, 2011). Both approaches are designed to employ a single form of inversion to recover the resistivity model from the AEM data. In this study, rather than developing a general methodology that can quantify uncertainty in AEM inverse problems, we focused on a specific issue, related to aquifer dynamics, identified by the local water agency in Butte and Glenn Counties in the Central Valley of California, U.S.A. In contrast to previous approaches, we employed multiple forms of inversion, using different types of data to inform the recovery of the resistivity model, and from those recovered resistivity models we derived many models displaying information about sediment type. This allowed us to explore the model space of the AEM data – consisting of the many resistivity and sediment-type models – and account for uncertainty in our analysis of the AEM data.

The study area covered two regions within Butte and Glenn Counties. There are various stratigraphic units in the study area that can include both aquifers and aquitards, resulting in considerable uncertainty in lateral and vertical extent of the hydrogeologic units represented in the Butte groundwater model (Butte County, 2008). The primary interest of the agency, in acquiring AEM data, was to obtain an improved delineation of the large-scale structure and heterogeneity of the aquifer system so as to better understand the extent of vertical connectivity. The existing groundwater model in the area, developed using well data, lacked sufficient detail to understand the connection between various depths within the aquifer system. Vertical head data from multi-completion wells could provide useful information but were only available at a limited number of locations. Vertical connectivity (or lack thereof) has important implications for groundwater management. For example, important questions surround the issue of how pumping from deeper portions might impact existing shallow wells. If groundwater conditions in shallow zones of the aquifer system are sufficiently connected to deeper zones, then high volume pumping by deep wells may impact users of groundwater in the shallower zones and may impact groundwater dependent ecosystems which are sensitive to conditions in the shallowest portions of the aquifer. Moreover, vulnerability of aquifer systems to cross-contamination depends strongly on connectivity. Understanding this component of aquifer dynamics will support better development of policies and strategies to manage groundwater sustainably for a diversity of water users and environmental needs. For example, this understanding could inform policies such as well permitting requirements for well construction, and could benefit assessment of a particular recharge project, vulnerability of groundwater dependent ecosystems, vulnerability to contamination, or the impacts of pumping on stream-groundwater interaction.

Working with AEM data acquired in the Butte and Glenn Counties, we developed an approach that allowed us to obtain specific information, from our interpretation of the AEM data, of direct relevance to addressing the identified issue in the study area. We developed an AEM interpretation workflow to generate an ensemble of resistivity models and corresponding sediment-type models from a combination of AEM data and existing well data (including resistivity logs and lithology logs). With this ensemble of models representing the model space of the AEM data, we explored the similarities and variability to first refine the understanding of the large-scale structure and heterogeneity in the aquifer system and then extracted information relevant to vertical connectivity. Of critical importance, we accounted for the dominant sources of uncertainty, captured in the model space in the inversion of the AEM data, and carried that uncertainty through to communicate the uncertainty in the obtained information. This provides the water managers with useful information, accompanied by an indication of the level of confidence they could place in the information. Designing an AEM interpretation workflow to address a specific issue of importance in understanding the dynamics of an aquifer system improves the way in which AEM data can be used to support both groundwater science and management.

2. Background

2.1 Hydrogeologic framework in study area

It is inappropriate to interpret any geophysical data without the benefit of knowledge about the geologic framework and its origins. The AEM method produces 3D models of electrical resistivity in the subsurface which can be transformed to sediment type (e.g., sand, gravel, clay, silt) due to the resistivity contrasts between the various sediment types. In general, coarse-grained materials (e.g., sand and gravel) are expected to have greater resistivity than fine-grained materials (e.g., silt and clay) due to smaller clay content or the greater pore volume containing the groundwater. The AEM method therefore cannot distinguish between geologic formations if there are similarities in sediment type due to their common alluvial/fluvial depositional environments. Nevertheless, it is very helpful in the study area to recognize two main stratigraphic units that will help delineate hydrogeologic units: (1) Pliocene-aged units, and (2) the overlying Quaternary-aged units (CDWR, 2014). Two Pliocene-aged units interfinger in the center of the study area: the Tuscan Formation in the east, and the Tehama Formation in the west (Ingersoll et al., 2016). These two units also contain informal lower and upper members that are more easily defined in the west. The overlying

Quaternary-aged units exist throughout most of the study area though stratigraphically pinch-out in the far eastern portion; they consist of the Red Bluff, Riverbank, and Modesto formations (Helley & Hardwood, 1985). A geologic cross section: B-B' illustrating these geologic formations are shown in Figure 1.

Fortunately, it is the differences in sediment type within and between formations (that are effectively highlighted by the AEM method) which best define the key hydrogeologic units in the study area. It is helpful to consider how sediment type differs in the western part from the eastern part of the study area (Greene & Hoover, 2014). A review of cross-sections developed using well data suggests three main zones in the aquifer system in the western part, which we here refer to as: lower, middle, upper. However, there is limited understanding of the lateral and vertical extent of these zones. The lower zone contains a coarse-grained and laterally continuous sand/gravel unit within the lower Tuscan Formation which abruptly transitions in the western part of the study area to the finer-grained and discontinuous channels of the lower Tehama Formation (Greene and Hoover, 2015). The middle zone is a mostly fine-grained unit containing upper Tehama/Tuscan deposits with discontinuous channelized sand bodies. The upper zone is mostly coarse-grained laterally continuous sand/gravel bodies of the upper Tuscan/Tehama as well as the Quaternary units (Ingersoll et al., 2016). The eastern portion of the study area contains the combined lower and upper Tuscan Formation overlain by sand/gravel bodies within the Quaternary units. The Tuscan deposits contain heterolithic units of sand/gravel channels interbedded with clay/silt zones as well as volcaniclastic debris-flow deposits (CDWR, 2014). The latter deposits add to the complexity of interpreting the AEM data to obtain information about the aquifer system due to their high resistivity (<500 Ωm) but lower permeability than the resistive (~50 Ωm) and permeable sand/gravel channels.

2.2 Introduction to the AEM method

2.2.1 Acquisition of data

The AEM method uses the electromagnetic induction phenomenon to obtain information about the electrical resistivity of the subsurface. Time-varying electric currents are injected through a transmitter loop attached to a helicopter (or small plane) to generate induced currents in the subsurface. These induced currents will depend upon the resistivity of the subsurface and generate an induced voltage that can be measured at a receiver loop. The link between electrical resistivity and sediment type is what was utilized in this study. The AEM method has been used in previous studies to map the large-scale architecture of an aquifer system (Knight et al., 2018; Meier et al., 2014; Podgorski et al., 2013; Sattel & Kgotlhang, 2004; Wynn, 2002).

In our study, we used a time-domain AEM system from SkyTEM (Sorensen et al., 2018). Measured induced voltages include multiple time channels that are normalized by the transmitter current and the area of the transmitter and receiver loops, resulting in the unit of $V/A\text{-}m^4$. The resolution of the AEM measurement depends upon various factors including the specific form of measurement given the AEM system, the resistivity of the subsurface, the noise level, and, in general, degrades with depth. With the SkyTEM system in our study area, where the AEM measurement was capable of resolving features to a depth of ~300 m, the horizontal resolution at the surface was about 40 m increasing to ~250 m at 300 m depth and the vertical resolution at the surface was about 2 m, increasing to ~40 m at 300 m depth. When measuring induced voltage from the subsurface at the receiver loop, a helicopter moves continuously along planned flight lines, and the raw voltages are stacked and referred to as the AEM sounding or AEM response at specific locations; the entire set of AEM soundings from the AEM survey are referred to as the observed AEM data.

2.2.2 Inversion of AEM data

To obtain a resistivity model of the subsurface from the observed AEM data, a spatially- (or laterally-) constrained inversion approach (Brodie & Sambridge, 2009; Kang et al., 2019; Viezzoli et al., 2008) has been widely used for hydrogeologic applications. This inversion takes into account the 3D nature of diffusive EM wave propagation but assumes the resulting model should display the layered structure of the subsurface. For each AEM sounding location, a 1D layered-resistivity model fitting the observed AEM response is sought. The spatial constraint, favoring a smooth transition of resistivity values between adjacent sounding locations, is implemented in the inversion through a regularization function. The regularization function also includes a reference model that can integrate prior information constraining the inversion based on ancillary data (e.g., well data), or an understanding of the expected variation of electrical resistivity in survey area (e.g., the average resistivity). The regularization function including both the spatial constraint and reference model is commonly referred to as the prior model for the inversion.

To provide an insight into what is sampled by an AEM measurement, we show in Figure 2a an example of a true resistivity model along a 1-km flight line. We simulated the acquisition of AEM data along this flight line with AEM sounding locations every 25 m. Shown in Figure 2b are the 1D layered-resistivity models recovered by inverting the AEM data, acquired at each sounding location, with the spatially-constrained inversion. The compilation of all these 1D models is referred to as the recovered resistivity model. We illustrate the issue of resolution in this figure by showing, in Figure 2a, the support volume of the central AEM sounding, i.e. the volume of the subsurface that contributes to the measured response at that sounding. Nabighian (1979) used the concept of a smoke ring to describe the volume within which the induced currents, generated by the AEM transmitter, propagate and diffuse in the subsurface. Although this support volume is shown in 2D, it is a 3D cone, with the bounding surface defining a 30 degree angle with the ground surface, and the diameter (commonly referred as the "AEM footprint") in this example, equal to about 25 m at the surface and ~700 m at 200 m below the surface. Horizontal and vertical length scales that can be resolved by the AEM method at depth is smaller than the supporting volume, but similarly decreases with depth. Because of this limited resolution of the AEM method, the recovered resistivity model in Figure 2b captures the large-scale resistivity structure and heterogeneity in the true resistivity model but increasingly loses the fine-scale structure as depth increases.

2.3 The source of the uncertainty in the recovered resistivity model

The AEM inverse problem, used to extract resistivity information from AEM data, is non-unique meaning that there are numerous resistivity models that can fit the observed AEM data. These numerous models define one component of the model space of the AEM data (the other components being the derived sediment-type and coarse-fraction models from the resistivity models); it is adequately exploring this model space that is an essential component of our workflow. The non-uniqueness of the inverse problem is closely related to the physics of the AEM method and results in the uncertainty in the recovered resistivity model. Therefore, it is important to understand the physics of the AEM method generating the uncertainty so as to set realistic expectations about what can be obtained from the inversion of AEM data.

We will describe, by generating synthetic AEM data, two well-known examples of sources of the non-uniqueness (e.g., Christensen & Lawrie 2012) and discuss their potential impact on our ability to extract information about the structure and heterogeneity of an aquifer system. For both examples we simulated the AEM response for a single layer embedded in a homogeneous background. The resistivity, thickness and depth to the top of the layer are denoted as ρ, h, and z, respectively; the resistivity of the homogeneous background is denoted as $\rho_{\mathrm{background}}$. To simulate the acquisition of the AEM data, a step-off waveform was used; where the step-off is defined as $1 - H(t)$, where $H(t)$ is the Heaviside step function. The simulation was conducted for co-located source and receiver loops, 40 m above the ground surface.

The first example demonstrates the inability to resolve differences in resistivity, once the resistivity is above a certain threshold; this is commonly referred to as a saturation of the resistivity. A simple 1D layered resistivity model was defined with a resistive layer of sand and gravel (ρ= 50 Ωm) embedded in a conductive background of clay and silt ($\rho_{\mathrm{background}}$= 20 Ωm); h and z were set equal to 20 m and 50 m, respectively, as shown in Figure 3a; the choice of resistivity values was based upon those determined by Knight *et al.* (2018) in the interpretation of AEM data from elsewhere in the Central Valley. The calculated AEM response from this model is presented as a black solid black line in Figure 3b. We then increased the resistivity of the layer from 50 Ωm to 100 Ωm, keeping other parameters the same, and calculated the AEM response (dashed line in Figure 3b). The AEM responses from the two resistivity models are almost identical indicating that there is no detectable difference in the AEM data. Even an increase in the resistivity of the layer to 1000 Ωm, caused a minimal change in the AEM response. This source of non-uniqueness makes it highly likely that an AEM inversion will underestimate the resistivity values corresponding to relatively resistive materials such as sand, gravel. We need to consider this when comparing a resistivity model from AEM data with other resistivity data (e.g., resistivity logs) and when transforming a recovered resistivity model from AEM data into sediment type.

The second example is the limitation in the ability to detect a layer, be it resistive or conductive, due to the diffusive nature of EM wave propagation. We refer to the required thickness of a layer, in order for it to be detected at a given depth, as the critical thickness; this thickness will increase with depth. We define a layer as being detectable if the addition of the layer, to a homogeneous background, results in a predicted change in the AEM response that is greater than 1%; we refer to this predicted change as the layer response. Given the typically assumed noise level of 3% in AEM data, this is a very conservative estimate, likely to underestimate the thickness that a layer must be in order to be resolved at a given depth. The layer response is calculated as follows

$$\text{Layer response (\%)} = 100 \times \sqrt{\frac{1}{n_{ch}} \sum_{i=1}^{n_{ch}} \left| \frac{F[\rho_{\mathrm{background}}] - F[\rho_{\mathrm{layer}}]}{F[\rho_{\mathrm{background}}]} \right|^2}, \tag{1}$$

where $F[\cdot]$ is a Maxwell operator which predicts the AEM response for a given 1D layered-resistivity model; ρ_{layer} is the 1D layered-resistivity model including the resistive layer; n_{ch} is the number of time channels in an AEM response.

Shown in Figure 4 is the critical thickness as a function of depth for a layer of sand/gravel in a clay/silt background and a layer of clay/silt layer in a sand/gravel background. Resistivity values of clay/silt and sand/gravel were assigned to be 20 Ωm and 50 Ωm, respectively. As expected, the critical thickness, regardless of composition, increases with depth, but the critical thickness of the sand/gravel layer is greater at all depths than that of the clay/silt layer indicating the higher sensitivity of the AEM data to a more conductive (i.e. clay/silt) layer. This limitation in resolving layers in the subsurface must be acknowledged in the interpretation of the AEM data.

2.4 Rock physics transform

The recovered resistivity model can be transformed to sediment type by constructing a relationship between sediment type and resistivity, with the information about sediment type obtained from the well data (Barfod et al., 2018; Foged et al., 2014; Knight et al., 2018). We adopted the approach of Knight et al. (2018) which begins with data pairs each composed of the resistivity value from a cell in the recovered AEM resistivity model and, from a nearby well, the corresponding section in a lithology log, where the descriptions of layers have been classified into a few discrete classes of sediment type appropriate for the study area. A linear equation is set up with the known resistivity value from the AEM resistivity model, known thicknesses of the AEM resistivity cell and each of the layers of sediments, and with unknown resistivity values for the sediment types. When setting up the linear equation, the physics of the AEM method is accounted for in a way that compensates for the resistivity saturation which underestimates the resistivity value of the more resistive materials. By repeating this process at all locations where there are data pairs, many linear equations are constructed. Solving this least-squares problem with bootstrapping generates the distributions of resistivity values that correspond to the defined sediment types. In order to determine an accurate resistivity-to-sediment-type transform, the location of wells with lithology data should be as close as possible to the AEM sounding locations (Knight et al., 2020). We designed the AEM survey with this goal in mind, resulting in 55 wells with lithology information within 100 m of an AEM sounding.

The above approach to constructing the resistivity-to-sediment-type transform maps each resistivity cell in the recovered resistivity model to one sediment type. There is an alternate way to transform the resistivity model to obtain information about the composition of the subsurface, and that is to capture information below the scale of the resistivity cell about the percentage of each sediment type that is present. Such an approach was recently taken in the interpretation of ground-based time-domain EM data (Goebel & Knight, 2020) and is directly applicable to AEM data. In this approach, it is assumed that there is finer-scale layering of sediment type, below the scale of the AEM resistivity cell. Random sampling of the resistivity distributions for various sediment types (determined using the above approach) is used to develop a relationship between resistivity and the percentage of one or more of the sediment types present. In this study, this approach provided a way to estimate the percentage of sand/gravel in a thick vertical interval, information relevant for assessing vertical connectivity within the aquifer system.

3. Available Data

Two AEM surveys were flown in parts of Butte and Glenn Counties in December 2018, using the SkyTEM 312 and 304 systems. Figure 5 shows the flight lines of the two AEM surveys. The SkyTEM 312 survey covers the western part of the study area, which includes the boundary between Butte and Glenn Counties, and the SkyTEM 304 covers the eastern part of the study area within Butte County. The length of the total flight lines is ~800 km, and the spacing between lines is ~500 m. Both SkyTEM systems are a dual moment system, which includes the low moment (LM) and the high moment (HM). The LM system can turn off the current in the transmitter loop much more rapidly than the HM system, so can obtain measurements at earlier time channels which contain more information in the near-surface region. The HM system uses a much higher current amplitude than the LM system, so can image to greater depths. Thus, by using both the LM and HM systems, we image near-surface structures as well as the deeper structures. System specifications of the two SkyTEM systems are summarized in Table 1. The AEM data were processed by Aqua Geo Framework (Asch et al., 2019).

Resistivity logs were available at 152 well locations, shown in Figure 5 as red circles; there are also drillers' logs at 21 of these locations shown as yellow circles. The harmonic and arithmetic average of resistivity values from the resistivity logs are 10 Ωm and 30 Ωm, respectively; these averages were taken to be the upper and lower limits of the average resistivity of the study area. The AEM surveys were designed to fly as close as possible to accurately located wells with lithology logs so as to construct an accurate resistivity-to-sediment-type transform. The result was a total of 55 wells with drillers' logs within 100 m of AEM sounding locations six of which were wells with resistivity logs; the locations of these wells, treated as co-located with the AEM soundings, are presented in Figure 5 as open triangles; so, a yellow circle containing a triangle and a red circle indicates a well location with a co-located lithology log as well as a resistivity log. We also had available in the study area twelve multi-completion wells, each composed of two wells with head measurements made in two screened intervals over the time period of 2013 to 2018; their locations are shown in Figure 5.

During the week of the AEM surveys (December 2018), water level measurements were made in 61 wells; their locations are shown in Figure 5 as blue solid circles. The top of the saturated zone (TSZ) in the study area was estimated by Dewar and Knight (2020) from the AEM data, first calibrating the method using water level measurements close to AEM soundings in the study area. This estimated TSZ was used in the process of transforming a resistivity model to a sediment-type model. In the study area, the TSZ was on average at a depth of 10 m, ranging from 3 m to 22 m.

For the classification of sediment type used in our study, the original descriptions in the lithology logs from the 55 wells were grouped into two units: sand/gravel and clay/silt. Both sand and gravel are aquifer materials, so they are combined into a single unit. The combining of clay and silt is due to the ambiguity in the original descriptions by drillers in the lithology logs as well as resistivity logs, where distinguishing between silt and clay is difficult, resulting in generalized categories that lump together the fines-dominated textures. In addition, there is often little motivation for the driller in accurately distinguishing between silt and clay, as they are both several orders of magnitude less permeable than sand and gravel, the primary materials of interest when drilling a well. A few of the logs describe materials related to a volcaniclastic debris-flow (lahar). While these materials make up an important facies, they are a minor portion of the lithologic logs (< 8%) and, because of their resistivity values, we are not able to distinguish them in the AEM data from the moderately resistive sand/gravel. We therefore excluded these materials from our classification system. When comparing the resistivity and lithology logs, we found a good correspondence in the logs between resistivity and sediment type, with sand/gravel corresponding to high resistivity values and clay/silt corresponding to low resistivity values.

4. AEM Interpretation Workflow

Our workflow, developed to obtain and interpret an ensemble of sediment-type models from AEM data and well data, included two main steps: the inversion of the AEM data and the resistivity-to-sediment-type transform, which is often referred to as a rock physics transform. In the AEM inversion step, we first sought to recover a resistivity model fitting the observed AEM data for a given prior model, then subsequently applied the posterior sampling to obtain multiple resistivity models. This procedure was repeated with a variable prior model. In the second step, we constructed a rock physics relationship between resistivity and sediment type to transform all of the resistivity models into models containing information about sediment type, and the percentage of sediment type. Interpretation of the models integrated prior knowledge of the aquifer system, which included head measurements from the multi-completion wells. We first describe how the workflow was implemented then present the results of the workflow.

4.1 Implementation of workflow

4.1.1 AEM inversion

The first step in our workflow is the inversion of the AEM data by using a spatially-constrained inversion (Viezzoli *et al.* 2008; Kang *et al.* 2019) to find a resistivity model which fits the observed AEM data for a given prior model, then applying the subsequent posterior sampling to obtain multiple resistivity models. This procedure is repeated with a variable prior model. We conducted six types of inversion, changing various parameters defining the prior model of the inversion algorithm so as to obtain six different resistivity models. These inversions are listed in Table 2 and discussed in more detail below.

We used no reference model in Inversion 1. Given the upper and lower limits of the average resistivity in the study area of 10 Ωm and 30 Ωm, respectively, we set the reference model equal to a homogeneous model with resistivity equal to 10 Ωm in Inversion 2, 20 Ωm in Inversion 3, and 30 Ωm in Inversion 4. In Inversions 5 and 6 we used the available resistivity logs to generate a reference model. In all inversions we assumed that there is a smooth transition between adjacent AEM soundings and the initial guess, m_0, was set to a homogeneous model with resistivity equal to10 Ωm. The Delaunay triangulation was used to find adjacent AEM soundings, as was done by Viezzoli *et al.* (2008). Adjacent soundings separated by a radial distance, *r*, greater than 1 km were neglected. For each of the AEM soundings, the same layering was used for the recovered resistivity model: 39 layers with a thickness starting at 3 m at the surface and then increasing by a constant factor of 1.07. The total number of sounding, $n_{sounding}$, was equal to 21,845, resulting in an inversion model, *m*, of the size 21,845 × 39 = 851,955 resistivity values.

Our regularization function, $\phi_m(m)$, can be written as

$$\phi_m(m) = \alpha_s \int \left(w_s\left(m - m_{ref}\right)\right)^2 dV + \alpha_r \int \left(\frac{dm}{dr}\right)^2 dV + \alpha_z \int \left(\frac{dm}{dz}\right)^2 dV \tag{2}$$

The first term (called smallness) is used to find a model close to the reference model, m_{ref}. The parameter, $w_s\,(x, y, z)$, by default set to 1, is a cell-based weighting function that allows the weighting of the reference model to vary throughout the survey area. This parameter was used to account for the distance between a cell in the resistivity model and the resistivity logs, which were used to define the reference model. The second and third terms quantify the variation in the radial direction (dm/dr) and the depth direction (dm/dz); these terms are often referred to as smoothness. Note these are all soft constraints with the alpha values, $\alpha_s, \alpha_r, \alpha_z$ determining the relative importance of each of the three terms. Values of α_r and α_z were fixed to 5 and 1 to indicate our preference to identify horizontally-continuous zones in the aquifer system. The value of α_s was varied to adjust the confidence we wish to place on the reference model. The alpha values used for all six inversions are given in Table 2. To generate the reference model used in Inversion 5 and 6, we interpolated the resistivity logs onto AEM cells using an inverse distance weighting; this resistivity model is referred to as ρ_{int}^{log}. The inverse distance weights calculated for the interpolation, w_{IDW}, was used as a cell-based weighting in Inversion 5 and 6; this effectively assigns higher confidence to cells of the reference model closer to the resistivity logs. In Figure 6 we visualize this process of generating the reference model from the resistivity logs.

To find an inversion model, m, which fit the observed AEM data and favored prior knowledge in the regularization function, $\phi_m(m)$, we used SimPEG, a Python-based open-source geophysics software package (Cockett et al., 2015; Heagy et al., 2017) to minimize the following objective function, $\phi(m)$:

$$\phi(m) = \phi_d(m) + \beta\phi_m(m) \tag{3}$$

subject to $\phi_d \leq \phi_d^*$

Here ϕ_d indicates data misfit, m is an inversion model, β is a trade-off parameter, and ϕ_d^* is a target misfit. The inversion iteration was started with the initial guess, m_0, and repeated until a good fit of the data was found ($\phi_d \leq \phi_d^*$). The initial β value, β_0, was estimated by a power method, then decreased with a constant factor (0.5) within the iteration to reduce the importance of the regularization term. For further information about the inversion method see Cockett et al., (2015) and Oldenburg & Li (2005).

Given the large range of resistivity values in the survey area, the distribution was best represented in logarithmic form; so, the inversion model was defined as:

$$m = \log(\rho^{-1}) = \log(\sigma), \quad m \in \mathbb{R}^M \tag{4}$$

where σ is electrical conductivity (S/m) and M is the number of the inversion model, m. The data misfit function was defined as

$$\phi_d(m) = \sum_{i=1}^{N} \left(\frac{F_i[m] - d_i^{obs}}{\epsilon_i} \right)^2, \tag{5}$$

where $F[\cdot]$ is a Maxwell's operator predicting AEM data for a given model, $d^{obs} \in R^N$ is the observed AEM data; N is the number of data. The standard deviation (or data error) of the i-th datum, ϵ_i, is defined as

$$\epsilon_i = \text{relative error (\%)} \times 0.01 \times \left| d_i^{obs} \right| \tag{6}$$

The relative error was set to 3%, and the target misfit, ϕ_d^*, was set to N.

The DOI was estimated, following Oldenburg & Li (1999), with a DOI threshold of 0.9. Two inversion models (Inversion 2 and 4 in Table 2) were used to calculate the DOI. The choice of the DOI threshold was based on the results of 1D AEM inversions shown in Appendix A.

We obtained a recovered model, m_* by solving the inverse problem shown in equation (4) then followed the approach of Rue (2001) and Fang *et al.* (2018) and drew samples from the posterior distribution, $\mathcal{N}(m_*, H_*^{-1})$. Here, $\mathcal{N}(m_*, H_*^{-1})$, indicates a multivariate Gaussian distribution with mean: m_* and covariance: H_*^{-1}. The Hessian matrix, $H_* \in \mathbb{R}^{M\times M}$ can be written as

$$H_* = J_*^T J_* + \beta_* W_m^T W_m, \tag{7}$$

where $J_* \in \mathbb{R}^{N\times M}$ is a sensitivity matrix: $J_* = W_d \frac{\partial F[m_*]}{\partial m_*}$ and W_m is a regularization matrix, which discretizes equation (2); $W_d = diag\left(\frac{1}{\epsilon_i}\right)$. Similar to Fang *et al.* (2018), β_* was set to $0.01 \times \beta_0$ to evaluate H_*.

Drawing a sample, m_s, from the distribution, $\mathcal{N}(m_*, H_*^{-1})$ can be written as

$$m^s = m_* + (L_*^T)^{-1} x \tag{8}$$

Here, the lower triangular matrix, L_*, is obtained by the Cholesky factorization of $H_* = L_* L_*^T$, and $x \in \mathbb{R}^M$ is a random vector drawn from $\mathcal{N}(0, I)$; $I \in \mathbb{R}^{M\times M}$ is an identity matrix. By repeating equation (8), n_{sample} times, we can obtain multiple samples, that can be readily transformed to resistivity models ($\rho_s = \exp(-m^s)$). For our application, we found that $n_{sample} = 1000$ was sufficient to approximate $m_* \simeq \frac{1}{n_{sample}} \sum_{k=1}^{n_{sample}} m_k^s$. This posterior sampling was repeated for each of six recovered resistivity models found with a variable prior model resulting in a total of 6006 resistivity models.

The spatially constrained AEM inversion algorithm and the posterior sampling method described in this section were implemented in a SimPEG-EM1D module (Kang et al., 2019). The SimPEG-EM1D code is publicly available through a github repository: https://github.com/simpeg/simpegEM1D.

When displaying the subsurface models in 3D, we interpolated them onto a 3D grid using an inverse distance weighting method, which is composed of uniform cells each with a dimension of 200 m×200 m×5 m in easting, northing, and depth direction, respectively. Our choice of the dimension was based upon spacing of the AEM flight lines, on average, ~500 m, and the smallest thickness of the resistivity cells, 3 m, at the surface.

4.1.2. Rock physics transform

We developed and applied two forms of the transforms to obtain information about sediment type from the resistivity models. One form was used to map each resistivity value to sediment type, defined as either sand/gravel or clay/silt. The other form was used to map resistivity to the percentage of sand/gravel.

4.1.2.1 Transform of resistivity cells to sediment type

Using the 55 pairs of co-located 1D layered-resistivity models and lithology logs (shown as open triangles in Figure 5), we used the method of Knight *et al.* (2018) to obtain the resistivity distributions corresponding to the two sediment types, sand/gravel and clay/silt. Given that water saturation will have a significant impact on the resistivity of lithologic units, we developed separate distributions for the sediment types above and below the top of saturated zone (TSZ), using the estimates of TSZ throughout the study area obtained by Dewar and Knight (2020). In this area the depth to the top of the TSZ ranged from 3-20 m.

Using the resistivity distribution for each sediment type above/below the TSZ, we chose the most likely sediment type for a given AEM resistivity value, $\rho^{AEM}\ (x, y, z)$. This transform function, $F_{sediment}[\cdot]$, can be written as

$$F_{sediment}[\ \rho^{AEM}\ ] = z^{AEM}, \tag{9}$$

where, $z^{AEM}(x, y, z)$ is a categorical variable distinguishing between the two sediment types: clay/silt ($z^{AEM} = 1$) and sand/gravel ($z^{AEM} = 2$).

Applying the rock physics transform to all 6006 resistivity models obtained from the previous step resulted in an ensemble of sediment-type models. Using them, we computed the probability of each sediment type:

$$P_{clay/silt} = \frac{\sum_{k=1}^{L} \delta^{AEM}(z_k^{AEM})}{L}, \tag{10}$$

$$P_{sand/gravel} = 1 - P_{clay/silt},$$

where δ^{AEM} is a Kronecker delta function: $\delta^{AEM}(z_k^{AEM}) = \begin{cases} 1, & z_k^{AEM} = 1 \\ 0, & z_k^{AEM} = 2 \end{cases}$; L is the number of the sediment-type models. Note that the obtained probabilities varied in 3D space (e.g.,

$P_{sand/gravel}\ (x, y, z)$). We define the level of uncertainty $UC_{sediment}$ as reaching a minimum at the two extreme values of $P_{sand/gravel}$ = 0 and $P_{clay/silt}$ = 1 as expressed below:

$$UC_{sediment} = \ (1 - |P_{sand/gravel} - 0.5| \times 2). \tag{11}$$

This uncertainty level in sediment type ranges from 0 to 1. The sediment-type models, along with calculated probabilities and uncertainty, were interpreted to obtain information about the large-scale structure of the aquifer system.

4.1.2.2 Transform of resistivity cells to coarse fraction

In order to obtain information about sediment type, below the scale resolved in the resistivity models, we used the approach of Goebel and Knight (2020). This allowed us to develop a transform between resistivity and the percentage of sand/gravel within the volume represented by a cell in the resistivity model; we refer to the percentage of the sand/gravel as the coarse fraction. Using the obtained resistivity distributions for the two sediment types we sampled from them with variable coarse fraction to construct a second transform function, $F_{\text{fraction}}[\cdot]$, which can be written as:

$$F_{\text{fraction}}[\ \rho^{AEM}\ ] = f_{\text{coarse}}^{AEM}, \tag{12}$$

where $f_{\text{coarse}}^{AEM}(x, y, z)$ is the resulting value of coarse fraction. Applying this rock physics transform to all 6006 resistivity models generated an ensemble of coarse-fraction models. A coarse-fraction model of the study area was used, along with the head data from the 12 multi-completion wells, to obtain information about the lateral variation in vertical connectivity within the aquifer system.

4.2 Results and discussion

4.2.1 Interpretation of sediment type models to obtain large-scale structure

Our interpretation workflow generated a model space that included 6006 resistivity models (6 recovered resistivity models and 6000 resistivity models from posterior sampling), and a corresponding 6006 models displaying sediment type and 6006 models displaying coarse fraction. In contrast to the approach typically taken in the interpretation of geophysical data (a single resistivity model with a single interpretation), this is an enormous model space that can be explored to address the issue that defined this study: an improved delineation of the large-scale structure and heterogeneity of the aquifer system so as to better understand the extent of vertical connectivity.

The six resistivity models, recovered using the parameters for the six inversions described in Table 2, all captured very similar large-scale structure, but varied significantly in areas where the AEM data were less sensitive. Given the high quality of the resistivity logs from the survey area, we felt that incorporating information from the logs in Inversion 6 significantly improved the accuracy of the recovered model. We show a three-dimensional view of the recovered resistivity model from Inversion 6 in Figure 7, displaying the subsurface variation in electrical resistivity in the study area. Given our level of confidence in this model, it was used to construct the rock physics transform. In Figures 8a and 8b, we show the resistivity distributions for clay/silt and sand/gravel, above and below the TSZ, respectively. The distributions clearly reveal the impact of water content on the resistivity distributions and emphasize the need to treat the regions above and below the TSZ separately. Higher values of resistivity values are found above the TSZ than below the TSZ due to the reduced water content. Below the TSZ, the resistivity distributions of the two units are well-separated, whereas above the TSZ significant portions of the distributions are overlapping, due to the impact of the variable water content. Using these distributions, we transformed all 6006 of the resistivity models into sediment-type models. The threshold values of 23 Ωm and 18 Ωm were used to separate resistivity values above and below the TSZ, respectively, into the two sediment types. The resistivity values in the recovered resistivity models ranged from 4 Ωm to 80 Ωm. The presence of values that fell outside of the distributions in Figure 8 was evidence that our transform did not sample all of the resistivity values in the study area. In order to address this, any resistivity value greater than those in the sand/gravel distribution was transformed to sand/gravel, and any resistivity value below those in the clay/silt distribution was transformed to clay/silt.

As representative of our model space, we show in Figure 9 vertical sections, along flight line L710601 (the red line in Figure 5), through the four resistivity models recovered from Inversion 1, 2, 4, and 6 in the left panel and the corresponding four sediment-type models derived from the recovered resistivity models in the right panel. The region below the DOI is shaded with a transparent white color. For comparison, in the left panel are shown 11 resistivity logs and in the right panel two lithology logs, all located within 200 m of the flight line. During the analysis of the lithology logs, and the development of the rock physics transform, we defined the units as sand/gravel and clay/silt. However, given the limited resolution of the AEM method, there is very likely clay/silt within the unit we would map as sand/gravel and vice-versa. We also knew that there was significant spatial heterogeneity within the aquifer system in this area, making it highly unlikely that thick homogeneous packages of sand/gravel or clay/silt would be present. We therefore, in interpreting sediment type models, referred to the two units as “sand/gravel-dominated” and “clay/silt-dominated.

In reviewing the four sediment-type models we observe similarities in the large-scale structure. On the western side there is a layer dominated by sand/gravel in the top ~100 m; this layer thins to the east and is absent on the eastern side of the models. The next layer is dominated by clay/silt, underlain (in three of the models) by a layer dominated by sand/gravel, shallowing towards the east. A comparison with the two lithology logs shows the ability of the AEM method to image large-scale packages but not the finer-scale variation as discussed in Section 2.3. Despite the similarities in the models, we can see in Figure 9 how the variation in the regularization function, used in the inversion, caused differences in the resistivity models and derived sediment-type models.

In Figure 9a we see a smooth layered structure in the resistivity model, and therefore in the derived sediment-type model. This reflects the emphasis put on the smoothness constraint in the regularization function and the lack of a reference model. In Figure 9b we see that adding a reference model of 10 Ωm, which corresponds to clay/silt in our rock physics transform, to the regularization function results in more resistivity values close to 10 Ωm, at depths below ~200 m. In this region, which includes the deepest part of the section designated as below the DOI, the AEM data have low sensitivity, so the inversion heavily weights the information contained in the regularization function. The impact of this is to increase, relative to Figure 9a, the amount of clay/silt-dominated material that is shown in the sediment-type model at depths below ~150 m. Similarly, in Figure 9c (Inversion 4), changing the reference model to 30 Ωm, which corresponds to sand/gravel-dominated in our rock physics transform, results in more resistivity values close to 30 Ωm below ~200 m; this increases the amount of the sand/gravel-dominated material below ~200 m. The fact that adding a reference model can completely change the sediment type is a good illustration of the high level of uncertainty that we face, and the importance of characterizing it, when deriving and interpreting a sediment-type model from AEM data.

While it is important to capture the uncertainty, it is equally important to recognize that adding relevant information to the inversion can improve the accuracy of the sediment-type model of the subsurface. This was demonstrated in conducting Inversion 6, where we used the interpolated resistivity logs as a reference model, with cell-based weighting. This constrained the inversion to find a resistivity model that not only fit the observed data, but also provided a good match with the resistivity logs. The result, as would be expected, was a much better match between this recovered resistivity model and the resistivity logs than was seen with the other resistivity models. More importantly, this model achieved improved agreement with the lithology logs. In particular, as shown in the right panel of Figure 9d, we see good agreement between the sediment type model and the lithology logs at the base of the top sand/gravel-dominated layer as well as at the top and base of the thick sand/gravel-dominated package underlying the clay/silt-dominated layer.

This exploration of the model space of the AEM data, positioned us to obtain information about the large-scale structure and heterogeneity in the aquifer system. Because of the high quality of the resistivity logs in the area, we selected the resistivity and sediment-type models derived from Inversion 6 to be the primary resistivity and sediment-type models. We interpolated the resistivity model onto the 3D grid using an inverse distance weighting and transformed all cells to sediment type. We then used the models in our model space, i.e., the 6006 resistivity models and derived/corresponding sediment type models, to quantify probabilities and uncertainty; the probability of sand/gravel-dominated and the uncertainty of sediment type were interpolated onto the 3D grid as well.

In Figure 10a we show the 3D primary sediment-type model displaying only those regions classified, through use of the transform, as being sand/gravel dominated; the DOI is presented as a blue transparent interface. In Figure 10b we show the same regions, displaying the probability of sand/gravel-dominated calculated using the other 6005 sediment type models, where the probability in a cell is equivalent to the percentage of models having the same sediment-type mapped in that cell. We see that the probability ranges from 30% to 100%, with the histogram of values shown in Figure 11. Recalling that this is a binary system in terms of sediment type, the sum of the probability of sand/gravel-dominated and the probability of clay/silt-dominated is equal to 100%.

The results derived from our AEM data were used to obtain information about the large-scale structure and heterogeneity within the aquifer systems. In Figure 10c, we show a vertical section through the model in Figure 10b with our interpretation. The model extends from the vertical section A-A’, the location of which is shown in Figure 5, and extends to the north. Seen in this section is the large-scale structure that we observed in the other sediment-type models shown in the right panel of Figure 9. As seen in the histogram, most of the probability values in the displayed regions are above 50% indicating that this structure is present in the majority of models. In the eastern part of the study area, there appears to be a continuous package of sand/gravel-dominated starting at the East-to-West (E-W) boundary and extending to the eastern limit of the study area; this E-W boundary separates eastern and western part of the region as shown in Figure 10c. We refer to this package of sand/gravel-dominated as the eastern zone; top and base of the eastern zone are mapped with red and yellow surfaces, respectively, in Figure 10c. In the western part of the study area, which corresponds to the westside of the E-W boundary, we identified three zones: an upper zone which is primarily sand/gravel-dominated, a middle zone which is primarily clay/silt-dominated, and lower zone which is primarily sand/gravel-dominated. The extent of these zones is shown in Figure 10c using three surfaces: the base of the upper, middle, and lower zones correspondingly represented as blue, red, yellow surfaces.

It is the information about probability, extracted from our model space, that we used to quantify the uncertainty, in each cell, in our ability to identify sediment type. When a cell has a probability of 100%, in terms of corresponding to one of the sediment types (sand/gravel or clay/silt), the uncertainty is defined as 0. As the probability, for either sediment type, moves towards 50%, the uncertainty increases, reaching a maximum of 1 when the probability of both sediment types equals 50%. This uncertainty is displayed in Figure 12. The dominant factor determining uncertainty is an inability to resolve the variation in resistivity; i.e. we cannot accurately determine the resistivity value in each cell. The ability to resolve the resistivity decreases with depth, with the DOI defined to indicate the depth at which we lose resolving ability. It is important to note that above the DOI there can be significant levels of uncertainty in areas where there is high spatial complexity so that resistivity is changing rapidly vertically and/or laterally. At the boundaries between the two sediment types, the smoothness constraint used in the inversion will result in recovered resistivity values close to the threshold resistivity value separating the two sediment types. Thus, small variations in recovered resistivity can easily change the resulting sediment type, determined from the transformation. This results in a high level of uncertainty in sediment type at any interface between the two sediment types.

The image of uncertainty in Figure 12 displays higher uncertainty with increasing depth but also maps surfaces displaying high uncertainty at shallower depths. The average uncertainty level of the lower zone, 0.6, was the highest of all the zones. This is an expected result because of the decreasing resolution of the AEM method with depth; a portion of the lower zone is below the DOI as shown in Figure 10b. Throughout the rest of the image, the changes and patterns we found in uncertainty indicate that the loss of resolution with depth was not the only control on the observed uncertainty. At the large scale, we found high uncertainty coincident with the surfaces defined as separating zones in the aquifer system. These surfaces separate zones dominated by different sediment types so, as described above, are expected to be surfaces of high uncertainty. At the smaller scale, within the zones, there are differences in both the average level and in the variability of the uncertainty which we also interpret as related to the presence of interfaces across which there are changes in sediment type. We found a moderate level of uncertainty in both the upper zone, 0.4, and the middle zone, 0.38. The fact that these uncertainty levels are very similar, not higher in the middle zone as would result from the degradation in resolution with depth, we attribute this to the presence of greater fine-scale variability in sediment type in the upper zone. The observed complex patterns in uncertainty within the upper zone indicate a complex interlayering of sand/gravel and clay/silt. The eastern zone has an average uncertainty value of

0.24 and shows a low level of uncertainty throughout the zone, suggesting less fine-scale spatial variability in sediment type compared to the other zones. The image of uncertainty in Figure 12 reveals numerous areas where we cannot interpret, with certainty, sediment type but we can interpret – with certainty – the presence of *changes* in sediment type, over short vertical distances.

4.2.2 Interpretation of coarse-fraction map to obtain information about vertical connectivity

The AEM method is limited in terms of the ability to resolve spatial variability in sediment type, but the recovered resistivity values will be highly sensitive to the volume fractions of the sediment types that are present. This can provide information about vertical connectivity in an aquifer system.

Using the primary resistivity model (from Inversion 6), we constructed the second form of the rock physics transform to map the percentage of the sand/gravel, referred to as the coarse fraction, at the resolution of the resistivity model. Figure 14a and 14b show the constructed transforms between resistivity values and coarse fraction above and below the top of the saturated zone (TSZ), respectively. The grey shaded region shows the standard deviation (i.e., 68% confidence interval), taken as the uncertainty of the transformed coarse fraction caused by variation in the resistivity distributions of the sediment types. The average standard deviation below the TSZ is 5%. The average standard deviation is higher above the TSZ, 24%. Given that the greater variation in the resistivity distributions is expected above the TSZ than below the TSZ, this higher standard deviation above the TSZ is an expected result. There are resistivity values beyond the range of the transform (e.g., 16 Ωm-22 Ωm below the TSZ). To address this, any value less than the lower limit was set to 0% coarse fraction and any resistivity value greater than the upper limit was set to 100% coarse fraction. The fact that there are resistivity values beyond the range of the transform shows the limitation of our approach. Thus, it is important not to interpret the absolute values displayed in coarse-fraction model, but to use the model in conjunction with available hydrological data (e.g., head data) to assess spatial heterogeneity in the area.

We transformed all resistivity models resulting in 6006 coarse-fraction models, then calculated the vertical average of the coarse fraction, between the TSZ and the base of the eastern zone in the eastern part of the study area, and between the TSZ and the base of the lower zone in the western part of the study area. When viewed in plan view, this provided vertically integrated coarse-fraction maps. The coarse-fraction map derived from the primary resistivity model is shown in Figure 14a; red lines contour the 50% coarse-fraction values. The standard deviation, obtained from the 6006 models, is shown in Figure 14b and represents uncertainty which is very low throughout most of the study area; white lines contour the 10% standard-deviation values. This is an expected result given that the AEM data has ability to resolve the percentage of sand/gravel for a thick vertical interval with good estimates of resistivity distributions for the sediment types. The black dashed line marks the separation between the eastern and western part of the study area, labeled as the E-W boundary in the figure; the Sacramento River is represented as the blue polygon.

The open circles shown in Figure 14a are the locations of the twelve multi-completion wells in the study area; these wells are labeled A to L, going from east-to-west. Each well is composed of two wells with head measurements made in two screened intervals. As an indication of vertical connectivity within the aquifer system, we calculated, for each multi-completion well, the minimum and maximum magnitude of the vertical head gradient, dh/dz between 2013 and 2018. As demonstrated by (Fogg, 1986), in heterogeneous, clastic sedimentary complexes such as this one, values of dh/dz vary strongly as a function of vertical connectivity, or the effective vertical hydraulic conductivities. Good connectivity produces lower values of dh/dz, approaching the lower values that typify horizontal gradients (dh/dx) that occur in the relatively well-connected, horizontally stratified packages of sedimentary facies. Poor vertical connectivity produces much higher values of dh/dz.

The solid circles showing the well locations in Figure 14a are color-coded to display the maximum $|dh/dz|$. The horizontal hydraulic gradients, dh/dx, in the study area are on the order of $\sim 10^{-3}$, so we interpreted dh/dz values close to this as indicative of good vertical connectivity, with connectivity decreasing as dh/dz increases (Fogg, 1986). In Figure 15 we plot the minimum and maximum $|dh/dz|$ versus the AEM-derived coarse fraction for the closest AEM sounding. The separation distance between an AEM sounding and a multi-completion well ranged from 22 m to 400 m. In both the map view in Figure 14a and the plot in Figure 15, we observe a correlation between the values of dh/dz and coarse fraction from the AEM data, with the general trend of decreasing vertical hydraulic gradient with increasing coarse fraction; an exception is the one outlier marked with red open rectangle (Well C).

We found low dh/dz values at monitoring wells A, B, and D in the eastern part of the study area. Figure 16 shows the hydrographs from Well A. Also shown are the layered-resistivity and sediment-type models from the closest AEM sounding and the resistivity and lithology logs from one of the wells in the multi-completion well; the TSZ and the base of the eastern zone are shown as black dashed lines. The two hydrographs are almost coincident, indicating good connectivity between the two depth intervals tapped by those wells; $\max(|dh/dz|)$ is 1.5×10^{-3}. Sediment type from the AEM data show a thick package of sand/gravel-dominated unit between the TSZ and the base of the eastern zone. Figure 14a shows that coarse fraction within the aquifer system is above 50% throughout most of the eastern area. This, combined with the well measurements, suggests that this is the region where we have the greatest vertical connectivity. The eastern area, interpreted from the AEM data to be a thick package of sand/gravel-dominated material, represents volcaniclastic materials derived from sources to the northeast. These include fluvial point-bars, channels and overbank deposits as well as debris flow deposits of the Tuscan and Quaternary formations.

In the western part of the aquifer system, we found coarse fraction values less than 50% in many areas and higher dh/dz values in the data from monitoring wells (G, H, I, J, K, L) in those areas than found in the eastern part. Shown in Figure 17 are two hydrographs from the shallower and deeper screened intervals in Well G. The different trends, particularly between 2013 and 2014, and the $\max(|dh/dz|)$ of 5.5×10^{-2} indicate poor connectivity. Both the AEM-based information and the logs show the presence of multiple clay/silt layers between the TSZ and the base of the lower zone.

The western part is where we identified the thick, clay/silt-dominated middle zone. This results in low coarse-fraction values which dominate the map pattern allowing more isolated fluvial systems (point-bars, channels, and overbank deposits) within the aquifer system to be highlighted. In particular, coarse fractions from the north-to-south trending Sacramento River system exist on the east side of the Easting line: 585000 m, while northwest-to-southeast oriented features from the Tehama and Quaternary formations (often called the Stony Creek system) are shown on the west side of this line.

Figure 18 shows the hydrographs and other data for Well C which, as seen in Figures 14a and 15, does not show the same correlation between dh/dz and coarse fraction as seen for the other wells. The magnitude of $\max(|dh/dz|)$ is 0.18, which indicates low connectivity. However, the layered-resistivity and sediment type models show the presence of a thick sand/gravel-dominated package between the TSZ and the base of the eastern zone. In the lithology log, however, there is a 5-m-thick clay/silt layer described at ~75 m depth. This clay/silt layer likely acts as a hydraulic barrier between the two screened intervals but was not resolved by the AEM method. As shown in Figure 4, the critical thickness at 75 m depth is ~5 m indicating a possibility of the AEM method to miss this layer.

There is not enough information available in the AEM data alone to make it possible to accurately quantify vertical connectivity within an aquifer system. We found, however, that deriving the coarse fraction from the AEM data provided an indicator of connectivity that could be used, in conjunction with well data, to assess the variability in connectivity throughout our study area.

5. Conclusions

We developed a methodology for the interpretation of AEM data that involved the use of multiple forms of inversion of the acquired AEM data and the development of derived models of sediment type and coarse fraction. Exploring this large model space allowed us to use the quantified uncertainty as an integral part of our interpretation of the derived models, and to communicate our level of confidence in the interpretation.

In the inversion of the data, we benefitted in the study area by having high quality resistivity logs available. The range of average resistivity from the resistivity logs was used to set a homogeneous reference model. We found that simply changing a resistivity value of a homogeneous reference model effectively changed the resulting resistivity values in the recovered resistivity model and transformed sediment type. This demonstrated the relatively high level of uncertainty present in the inversion step of the workflow. Using the interpolated resistivity logs as a reference model improved the accuracy of the sediment-type model, thus demonstrating the value of incorporating high quality ancillary data in the inversion. The recovered resistivity model from this inversion was used to develop our primary sediment-type model.

We first used the primary sediment-type model to interpret the large-scale structure of the aquifer system and used all of the models in the model space to quantify uncertainty. The observed uncertainty gave us confidence in our interpretation of the large-scale structure and also provided additional information about subsurface heterogeneity. Not surprisingly, regions below the DOI showed high levels of uncertainty. What our methodology revealed, however, were areas with high levels of uncertainty across the entire depth range of our models. The uncertainty was highest along surfaces where the resistivity values were very close to the cut-off between the resistivity ranges corresponding to the two sediment types. In this way, the sediment-type models displaying high levels of uncertainty over short vertical distances, displayed – with certainty – interfaces across which sediment type was changing. This is a new form of interpretation of AEM data that can be used to assist in the mapping of large-scale structure, and to identify regions where there is significant finer scale interlayering of different sediment types.

The motivating issue in this study was to develop an improved understanding of the vertical connectivity of the aquifer system. We used vertical head gradient data from 12 multi-completion wells to obtain independent indicators of connectivity at 12 locations that helped corroborate the results derived from the geophysical data, and enrich our interpretation. We transformed the resistivity values from the primary recovered resistivity model to the percentage of sand/gravel, and from this obtained a plan view of integrated coarse fraction across the depth range of the imaged aquifer system. We found a correlation between coarse fraction and vertical head gradient, that suggests that the coarse-fraction maps, derived from AEM data, can be used to bridge the data gap between sparse multi-completion wells. When combined with the interpreted large-scale structure, these maps could also be used to prioritize the locations of new monitoring wells to obtain a more complete understanding of the vertical connectivity within the aquifer system.

The AEM method can provide valuable information about aquifer systems and thereby benefit management efforts. The focus of our research is to develop ways of maximizing the information about aquifer systems that can be obtained from AEM data while capturing and communicating the relevant uncertainty. We advocate an approach that works with an extensive model space, so that mapping of uncertainty can become the standard practice when interpreting AEM data. As we found in this study, quantifying uncertainty can be used not only to communicate the level of confidence in the identification of sediment type, but can assist in identifying interfaces between sediment type, at both the large and fine scale. Continued research, focused on exploring the optimal way to interpret AEM data, and integrate these data with other forms of hydrologic data, will undoubtedly lead to the increased adoption of the AEM method as an integral component of subsurface characterization for groundwater science and management.

Acknowledgments, Samples, and Data

Funding for this research was provided by the Ministry of Environment and Food of Denmark, the Ecoinnovation Programme (grant no. MST-117-00388), the California Department of Water Resources (grant no. 4600012515) through the Stanford Groundwater Architecture Project (https://mapwater.stanford.edu/), and the Gordon and Betty Moore Foundation (grant no. GBMF6189). We would like to thank Aqua Geo Frameworks for providing the processed AEM data. We thank Sharla Stockton from Glenn County for providing constructive discussion about the hydrogeology of the study area. We also thank Noah Dewar from Stanford University for providing the estimate of top of the saturated zone in the study area. We are grateful to the SimPEG community for developing and publicly releasing the SimPEG-EM1D module used in this study.

Datasets for this research are owned by Department of Water Resources (DWR), Calfornia and currently available through Asch et al., (2019), but will also be available through the DWR’s open data portal.

Appendix A. 1D AEM Inversions with a Single Sounding

In this appendix, we describe how we selected the inversion parameters presented in Table 2 with a 1D AEM inversion analysis. We used a single AEM sounding with the closest separation distance from a well location marked as open rectangle in Figure 5 (wellID: 21N01W11A001M); this separation distance is 24 m. Both lithology and resistivity logs are available at this well, and they are shown in Figure A1. We applied the workflow to the AEM response from a single sounding location. The first step is inverting AEM response. Prior information used for 1D AEM inversions is the following. First, a general conceptual model in the Central Valley where the study area is located is the presence of sand/gravel (resistive) channels embedded in a clay/silt (conductive) background (Faunt, 2010); this was used to determine the initial guess of the inversion. Second, the range of the average resistivity from the resistivity logs in the study area is: 10 Ωm-30 Ωm; this was used to generate a homogenous reference model. Third, the closest resistivity log from the AEM sounding shown in Figure A1 was used to generate an inhomogeneous reference model.

We performed three stages of 1D AEM inversions by altering prior models. We started our first stage of AEM inversions with a minimal prior information only using the smoothness term in equation 2. In the second stage, we added a homogenous reference model using the range of the average resistivity. As shown in Figure A1, the resistivity log was upscaled to the layer used for the AEM inversion, used as a reference model in the third stage.

For the first stage of inversions α_s and α_z were set to 0 and 1, respectively; α_s = 0 indicates there is no influence from a reference model. We ran three inversions with variable starting models: 10 Ωm, 20 Ωm, 30 Ωm based upon the range of the average resistivity. Figure A2 shows recovered layered-resistivity models; the upscaled resistivity log is shown together for comparison with the recovered models. Overall, all three models are very similar indicating that inversions are insensitive to an initial model. Based upon that we fixed the initial model, m_0, as 10 Ωm for following inversions. Given that the clay/silt is the background materials, the lower limit of the average resistivity, 10 Ωm, was chosen as the initial model.

In the second stage, we added a homogeneous reference model. For this, α_s value was increased from 0 to 1; α_z was kept as 1 indicating relative importance of the smoothness and the smallness terms are about the same. We ran three inversions with variable reference models: 10 Ωm, 20 Ωm, 30 Ωm. Figure A3 shows recovered layered-resistivity models. In top 200 m, three resistivity models are similar, whereas they show significant differences below 200 m. This indicates a high level of the uncertainty below 200 m. The recovered resistivity value gets closer to the reference model as the depth increases. This reflects decreasing sensitivity of AEM response with depth. For deep layers having a low sensitivity of AEM response, our inversion was constrained to put resistivity values close to the reference model. This was a fundamental idea for Oldenburg & Li (1999) to compute DOI, which indicates the depth at which we lose resolving ability. We followed this approach, and compared the calculated DOI with another well-known approach from Vest Christiansen & Auken (2012), which have been widely used in AEM inversions for hydrogeologic applications.

The DOI approach from Oldenburg & Li (1999) requires carrying out two inversions with different reference models: m_{ref}^1 and m_{ref}^2; resulting inversion outputs are m_*^1 and m_*^2. Then DOI index can be computed as

$$\text{DOI index} = \frac{m_*^1 - m_*^2}{m_{ref}^1 - m_{ref}^2} \tag{A1}$$

To calculate the DOI, we selected the two recovered layered-resistivity models, which used 10 Ωm and 20 Ωm as the reference models; so, m_{ref}^1 and m_{ref}^2 are 10 Ωm and 20 Ωm, respectively. To decide the DOI, a threshold value for the DOI index needs to be chosen, and this process is somewhat arbitrary; any value can be chosen between 0 and 1. DOI index of 0 means that the ability to resolve structure is high, whereas that of 1 means that the lack ability to resolve structure. We calculated the DOI with two threshold values: 0.4 and 0.9, and calculated DOI values were: 280 m and 353 m, respectively. The DOI calculated from Vest Christiansen & Auken (2012)'s approach was 271 m with their threshold value of 0.8; this value matches well with our DOI with threshold value of 0.4, 280 m. A threshold value of the DOI was determined later in this appendix after we finished the final stage of inversions.

For the final stage of inversions, we used the upscaled resistivity log shown in Figure A1 as a reference model. It is important to recognize that the supporting volume of the resistivity log is much smaller than that of the AEM data (see Figure 1a). Thus, the resistivity log is not a perfect representation of the true resistivity model that we seek in our AEM inversion. The reference model should be viewed as a soft constraint, that is the inversion is not forcing the recovered layered-resistivity model which is the same as the reference model. Our confidence of the reference model can be adjusted with α_s. We ran two inversions with different α_s values: 0.1 and 1, and show the results in Figure A5. Both of the recovered layered-resistivity models are much closer to the upscaled resistivity log compared to the models from the previous inversions. A higher α_s value reinforces the inversion to be closer to the reference model. Note that even when we set the α_s value to 1, the recovered layered-resistivity model is not exactly the same as the upscaled resistivity log, which indicates the trade-off made in the inversion to fit the data while preserving structures in the reference model.

From a total of the eight recovered layered-resistivity models, we removed the two from the first stage which did not show major differences, resulting in a total of six recovered models; these two models correspond to Figures A2b and A2c. In Figure A6, we show the remaining six recovered layered-resistivity models. Red and blue lines distinguish whether the upscaled resistivity log was used as a reference model or not. The two DOI estimates with different threshold values are also shown as dashed lines. In the top 200 m, all six resistivity models are compatible except for a few minor features: underestimated resistivity values for shallow resistor in the top 30 m and missing a thin resistor at 60 m depth indicating a lower level of uncertainty in the top 200 m than below 200 m. However, below 200 m, the layered-resistivity models show large differences indicating a higher level of uncertainty. Imaging the thick resistor at 230 m depth was not possible without the resistivity log information, even though its top boundary was located above the DOIs. However, with the resistivity log information, we were able to image this thick resistor. Given that we have successfully incorporated the resistivity log information, we selected 0.9 as our threshold value for calculating the DOI.

REFERENCES

Asch, T. H., Abraham, J. D., & Cannia, J. C. (2019). *Hydrogeologic Framework of Selected Areas in Butte and Glenn Counties, California*. Butte County.

Auken, E., Christiansen, A. V., Kirkegaard, C., Fiandaca, G., Schamper, C., Behroozmand, A. A., et al. (2015). An overview of a highly versatile forward and stable inverse algorithm for airborne, ground-based and borehole electromagnetic and electric data. *Exploration Geophysics*, *46*(3), 223–235. https://doi.org/10.1071/EG13097

Barfod, A. A. S., Møller, I., Christiansen, A. V., Hoyer, A. S., Hoffimann, J., Straubhaar, J., & Caers, J. (2018). Hydrostratigraphic modeling using multiple-point statistics and airborne transient electromagnetic methods. *Hydrology and Earth System Sciences*. https://doi.org/10.5194/hess-22-3351-2018

Brodie, R., & Sambridge, M. (2009). Holistic inversion of frequency-domain airborne electromagnetic data with minimal prior information. *Exploration Geophysics*, *40*(1), 8–16. https://doi.org/10.1071/EG08110

CDWR. (2014). *Geology of the Northern Sacramento Valley*. *California Department of Water Resources*. California: Sacramento.

Christensen, Minsley, & Christensen. (2017). Generation of 3-D hydrostratigraphic zones from dense airborne electromagnetic data to assess groundwater model prediction error. *Water Resources Research*. https://doi.org/10.1002/2016WR019141

Christensen, N. B., & Lawrie, K. C. (2012). Resolution analyses for selecting an appropriate airborne electromagnetic (AEM) system. *Exploration Geophysics*, *43*(4), 213–227. https://doi.org/10.1071/EG12005

Cockett, R., Kang, S., Heagy, L. J., Pidlisecky, A., & Oldenburg, D. W. (2015). SimPEG: An open source framework for simulation and gradient based parameter estimation in geophysical applications. *Computers & Geosciences*, *85*, 142–154. https://doi.org/http://dx.doi.org/10.1016/j.cageo.2015.09.015

Dewar, N., & Knight, R. (2020). Estimation of the top of the saturation zone from airborne electromagnetic data. *Geophysics*, *85*(8), EN63–EN76.

Fang, Z., Da Silva, C., Kuske, R., & Herrmann, F. J. (2018). Uncertainty quantification for inverse problems with weak partial-differential-equation constraints. *Geophysics*, *83*(6), R629–R647. https://doi.org/10.1190/geo2017-0824.1

Faunt, C. C. (2010). *Groundwater availability of the Central Valley aquifer, California*. *California Water Crisis*.

Foged, N., Marker, P. A., Christansen, A. V., Bauer-Gottwein, P., Jørgensen, F., Høyer, A. S., & Auken, E. (2014). Large-scale 3-D modeling by integration of resistivity models and borehole data through inversion. *Hydrology and Earth System Sciences*, *18*(11), 4349–4362. https://doi.org/10.5194/hess-18-4349-2014

Fogg, G. E. (1986). Groundwater Flow and Sand Body Interconnectedness in a Thick, Multiple-Aquifer System. *Water Resources Research*, *22*(5), 679–694. https://doi.org/https://doi.org/10.1029/WR022i005p00679

Goebel, M., & Knight, R. (2020). Recharge Site Assessment Though the Integration of Surface Geophysics and Cone Penetrometer Testing. *Geophyics*.

Greene, T. J., & Hoover, K. (2014). Hydrostratigraphy and Pump-test Analysis of the Lower Tuscan/Tehama Aquifer, Northern Sacramento Valley, CA.

Heagy, L. J., Cockett, R., Kang, S., Rosenkjaer, G. K., & Oldenburg, D. W. (2017). A framework for simulation and inversion in electromagnetics. *Computers & Geosciences*, *107*, 1–19. https://doi.org/https://doi.org/10.1016/j.cageo.2017.06.018

Helley, E. J., & Hardwood, D. S. (1985). *Geologic Map of the Late Cenozoic Deposits of the Sacramento Valley and Northern Sierran Foothills, California: U.S. Geological Survey Miscellaneous Field Studies Map MF-1790*.

Ingersoll, R. V, Steinpress, M. G., & Spangler, D. (2016). Application of actualistic sand petrofacies in hydrogeology: An example from the northern Sacramento Valley, California, USA. *GSA Bulletin*, *128*(3–4), 661–668. https://doi.org/10.1130/B31334.1

Kang, S., Fournier, D., Werthmüller, D., Heagy, J. L., & Oldenburg, W. D. (2019). simpegEM1D: gradient-based 1D inversion for large-scale airborne electromagnetic data. In *AGU annual meeting 2018*.

Knight, R., Smith, R., Asch, T., Abraham, J., Cannia, J., Viezzoli, A., & Fogg, G. (2018). Mapping Aquifer Systems with Airborne Electromagnetics in the Central Valley of California. *Ground Water*. https://doi.org/10.1111/gwat.12656

Meier, P., Kalscheuer, T., Podgorski, J. E., Kgotlhang, L., Green, A. G., Greenhalgh, S., et al. (2014). Hydrogeophysical investigations in the western and north-central Okavango Delta (Botswana) based on helicopter and ground-based transient electromagnetic data and electrical resistance tomography. *Geophysics*, *79*(5), B201–B211. https://doi.org/10.1190/geo2014-0001.1

Minsley, B. J. (2011). A trans-dimensional Bayesian Markov chain Monte Carlo algorithm for model assessment using frequency-domain electromagnetic data. *Geophysical Journal International*, *187*(1), 252–272. https://doi.org/10.1111/j.1365-246X.2011.05165.x

Oldenburg, D. W., & Li, Y. (1999). Estimating depth of investigation in dc resistivity and IP surveys. *Geophysics*, *64*(2), 403–416.

Oldenburg, D. W., & Li, Y. (2005). 5. Inversion for Applied Geophysics: A Tutorial. In *Near-Surface Geophysics* (Vol. 5, pp. 89–150). https://doi.org/10.1190/1.9781560801719.ch5

Podgorski, J. E., Auken, E., Schamper, C., Vest Christiansen, A., Kalscheuer, T., & Green, A. G. (2013). Processing and inversion of commercial helicopter time-domain electromagnetic data for environmental assessments and geologic and hydrologic mapping. *Geophysics*, *78*(4), E149–E159. https://doi.org/10.1190/geo2012-0452.1

Rue, H. (2001). Fast sampling of Gaussian Markov random fields. *Journal of the Royal Statistical Society: Series B (Statistical Methodology)*, *63*(2), 325–338. https://doi.org/10.1111/1467-9868.00288

Sattel, D., & Kgotlhang, L. (2004). Groundwater Exploration With Aem in the Boteti Area, Botswana. *Exploration Geophysics*, *35*(2), 147–156. https://doi.org/10.1071/EG04147

Sorensen, K. I., Auken, E., & Auken, E. (2018). SkyTEM – a New High-resolution Helicopter Transient Electromagnetic System SkyTEM – a new high-resolution helicopter transient electromagnetic system, *3985*. https://doi.org/10.1071/EG04194

Vest Christiansen, A., & Auken, E. (2012). A global measure for depth of investigation. *Geophysics*, *77*(4), WB171–WB177. https://doi.org/10.1190/geo2011-0393.1

Viezzoli, A., Christiansen, A. V., Auken, E., & Sørensen, K. (2008). Quasi-3D modeling of airborne TEM data by spatially constrained inversion. *Geophysics*, *73*(3).

Wynn, J. (2002). Evaluating groundwater in arid lands using airborne magnetic/EM methods: An example in the southwestern U.S. and northern Mexico. *The Leading Edge*, *21*(1), 62–64. https://doi.org/10.1190/1.1445851

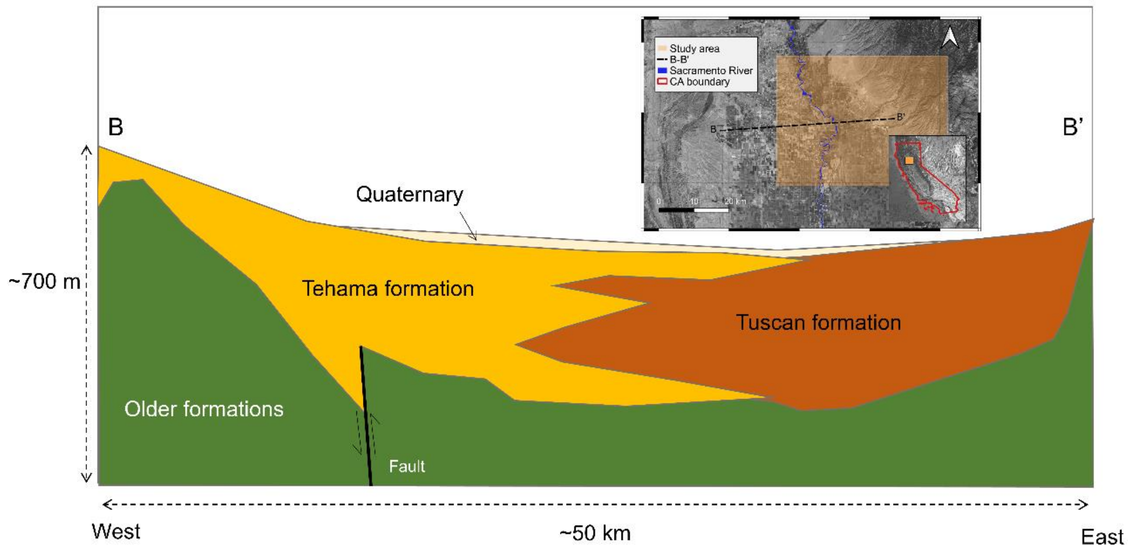

Figure 1. A geologic cross section: B-B’ illustrating geology of Butte and Glenn Counties, California, U.S.A. Modified from CDWR (2014). An inset map shows the location of the cross section: B-B’.

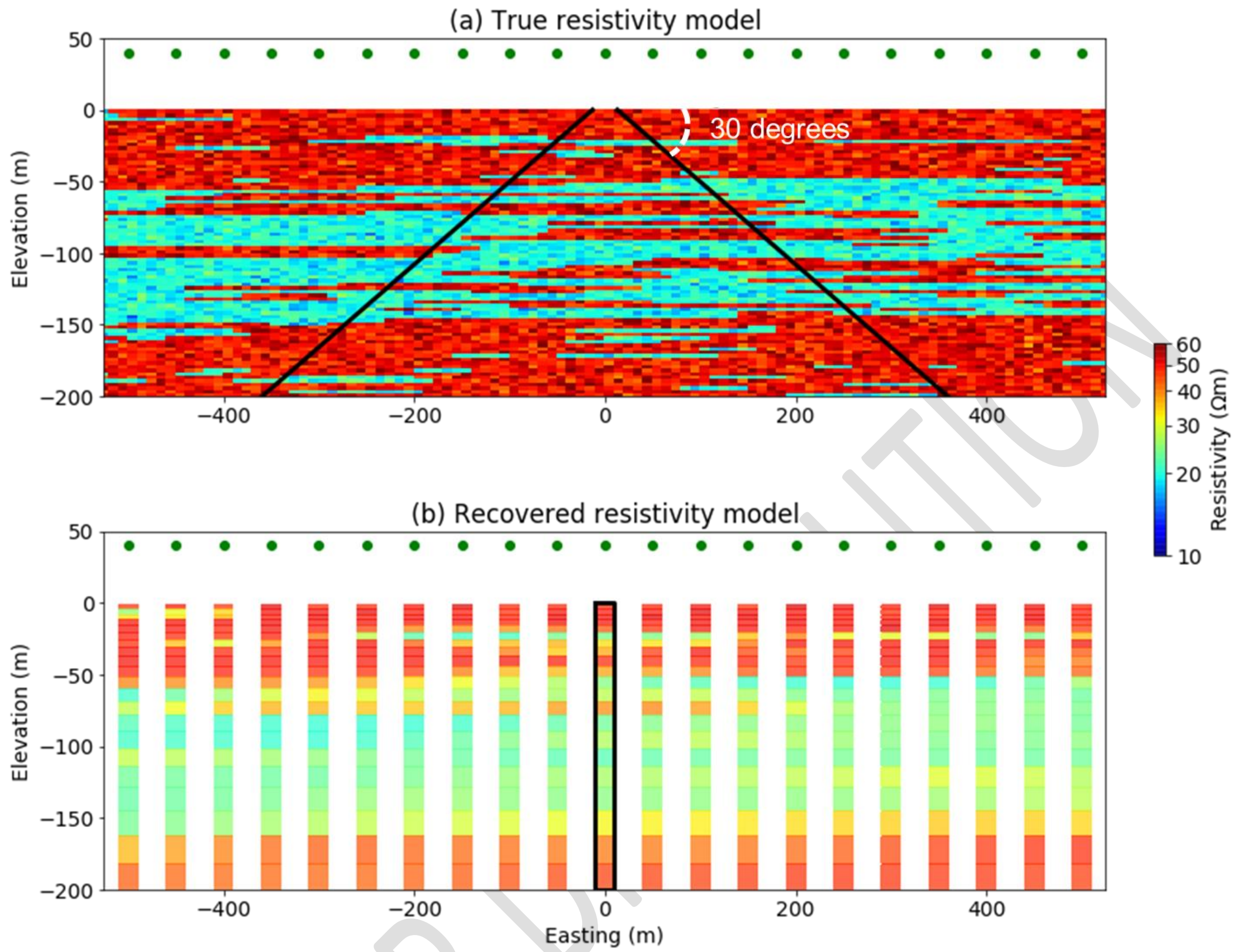

Figure 2. Conceptual diagram illustrating the recovered resistivity model from the 1D spatially-constrained inversion. (a) The true resistivity model along a 1 km flight line. Black lines indicate the cylindrical support volume of the AEM response at the center sounding location. (b) The 1D recovered resistivity models. Green dots show locations of the twenty-one AEM soundings with 25 m interval and 40 m flight height. The 1D layered-resistivity model at the center sounding location is enclosed with a black rectangle.

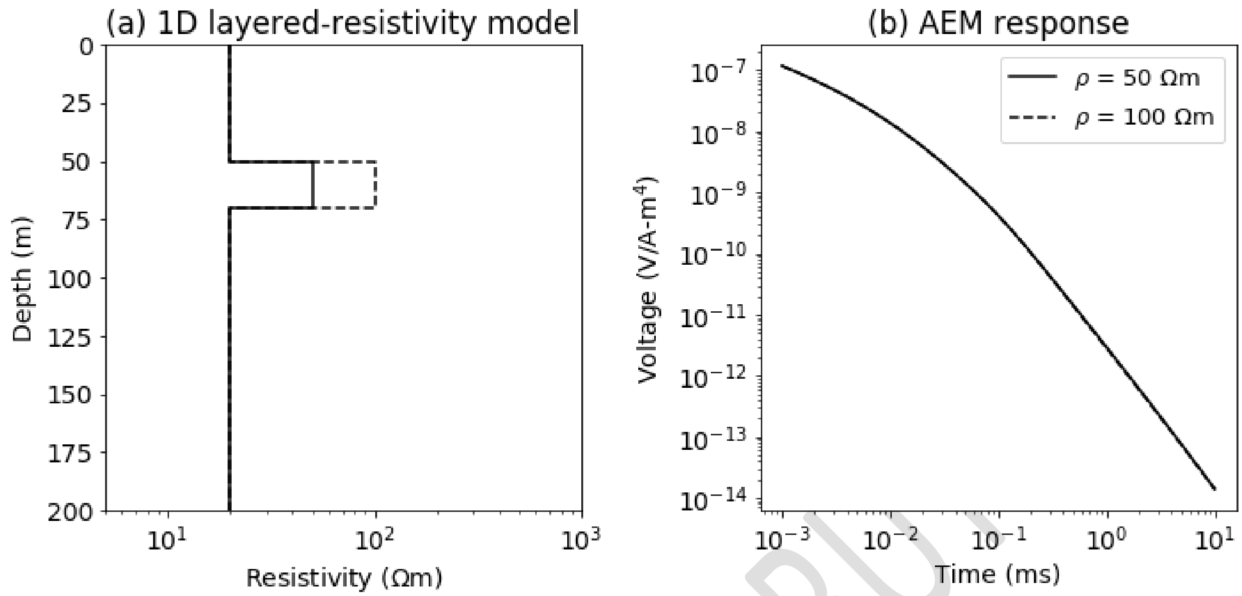

Figure 3. An example illustrating a source of non-uniqueness in AEM inversion due to the inability to resolve differences in resistivity, once the resistivity is above a certain threshold. (a) 1D layered resistivity models. The solid and dashed lines represent two models with a different resistivity value (ρ) for the layer: 50 Ωm and 100 Ωm. For both models the depth to the top of the layer is 50 m and the thickness of the layer is 20 m. (b) AEM responses corresponding to the models in Figure 3a.

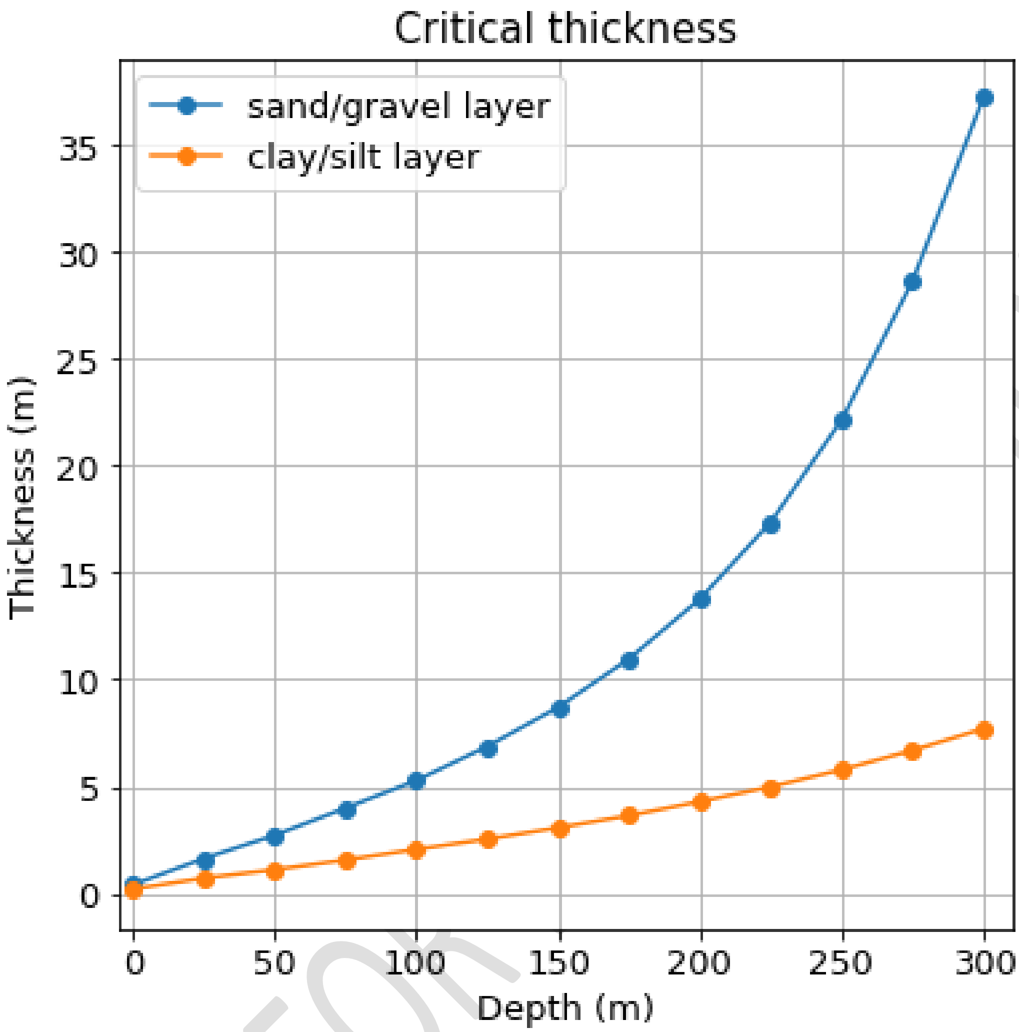

Figure 4. The critical thickness of a layer as a function of depth. The critical thickness is the required thickness of a layer, embedded in a homogenous background, in order for the layer to be detected by AEM data. Blue curve: a sand/gravel layer in clay/silt background. Orange curve: a clay/silt layer in a sand/gravel background. The resistivity values used for clay/silt and sand/gravel were 20 Ωm and 50 Ωm, respectively.

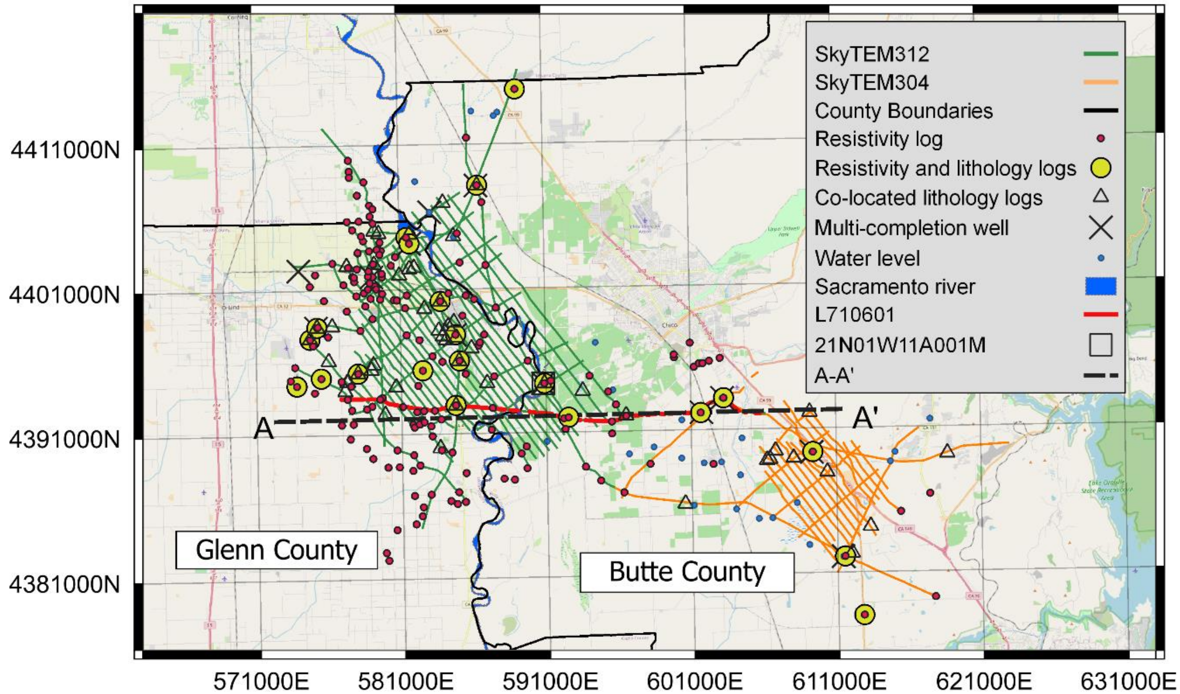

Figure 5. Location map of Butte and Glenn Counties in Central Valley of California showing available data. Light green and orange lines indicate two AEM surveys flown with SkyTEM 312 and 304 systems, respectively. Black lines show the county boundaries. Red circles show 152 resistivity logs; 21 of them also having drillers logs are denoted as yellow circles. Open triangles show 55 well locations containing lithology logs within 100 m separation distance from AEM soundings; these well locations were treated as co-located with AEM soundings. Blue circles show the location of 61 wells with measured water levels during the same week of the AEM survey. Cross marks indicate the location of 12 multi-completion wells. Blue polygon indicates the Sacramento River. The red line indicates an AEM flight line (lineID: L710601). A-A' shown as a black dashed line indicates horizontal location of a vertical section shown in Figures 10c and 12. An empty rectangle shows a well location (wellID: 21N01W11A001M) including both resistivity and lithology logs.

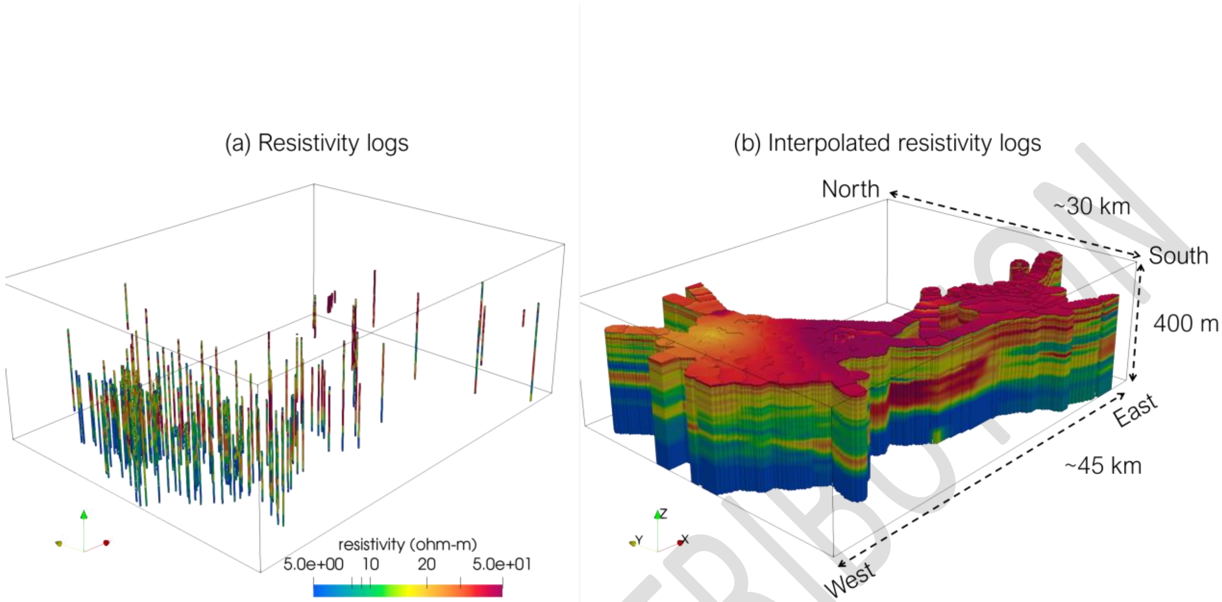

Figure 6. Interpolation of resistivity logs. (a) Resistivity logs at 152 well locations. (b) 3D interpolated volume of the resistivity displaying result of the interpolation. The resistivity logs were interpolated to the discretized layers at all sounding locations resulting in ρ_{int}^{log} . For a visualization purpose, we interpolated the ρ_{int}^{log} to the 3D grid as shown in Figure 6b.

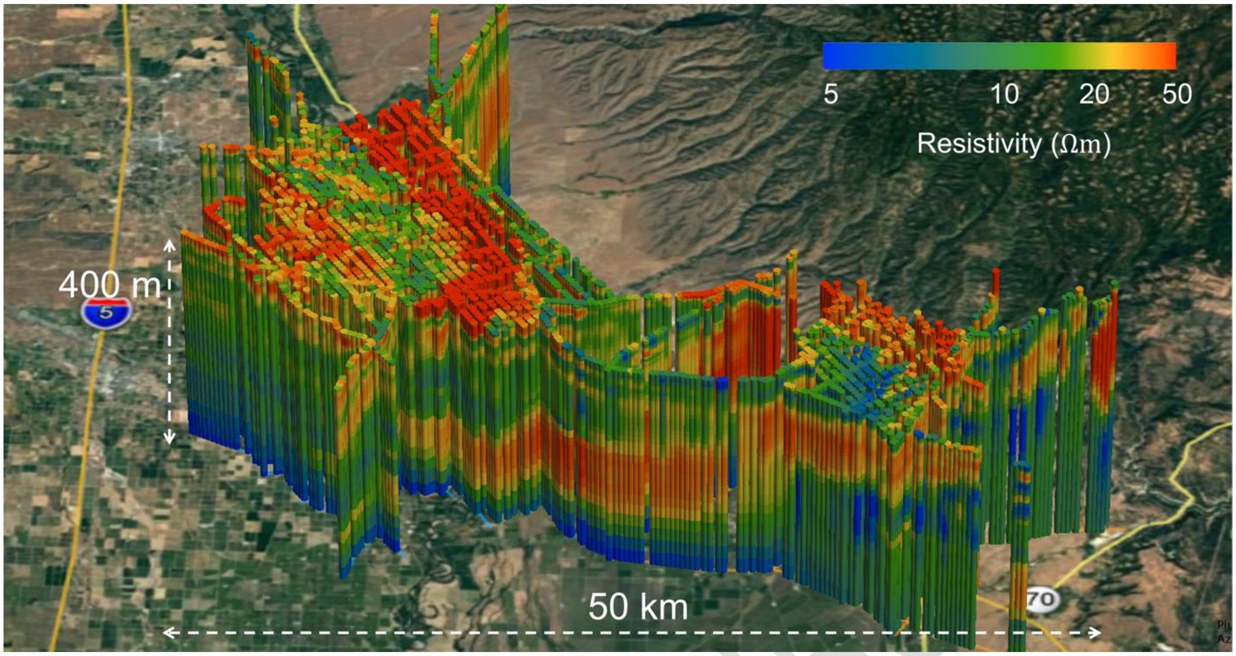

Figure 7. Three-dimensional display of subsurface variation in electrical resistivity in Butte and Glenn Counties in the Central Valley of California, U.S.A., obtained through the processing and inversion of AEM data. The inverted 1D resistivity models imaging the top ~400 m of the subsurface in the study area are displayed at AEM sounding locations. This resistivity model corresponds to Inversion 6 in Table 2.

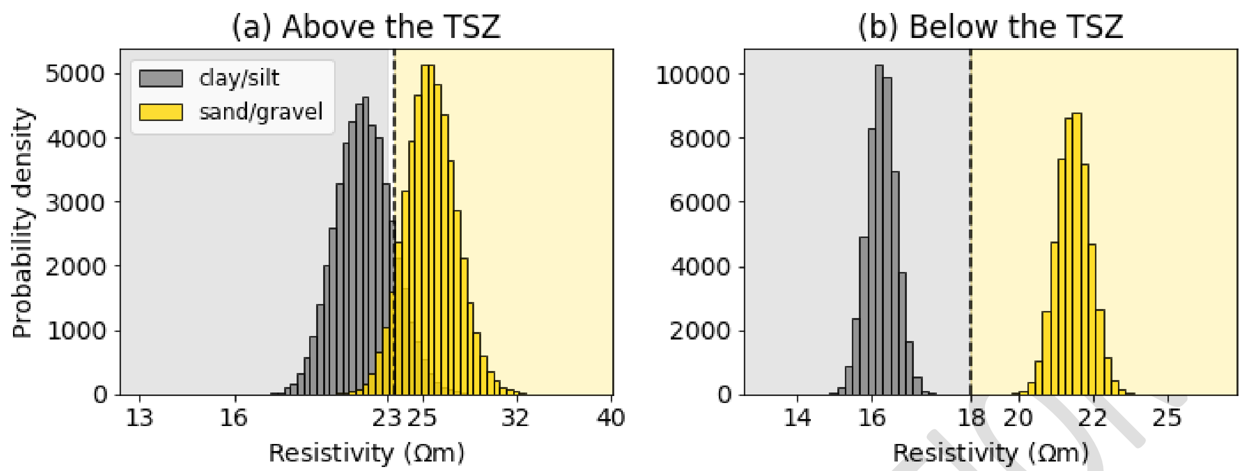

Figure 8. Resistivity distributions of clay/silt and sand/gravel obtained from the rock physics transform. (a) Above the top of the saturated zone (TSZ). (b) Below the TSZ. Grey and yellow colors indicate clay/silt and sand/gravel, respectively. Vertical dashed lines denote threshold values of resistivity used to transform resistivity values from AEM to the two sediment types; these threshold values above and below the TSZ are 23 Ωm and 18 Ωm, respectively.

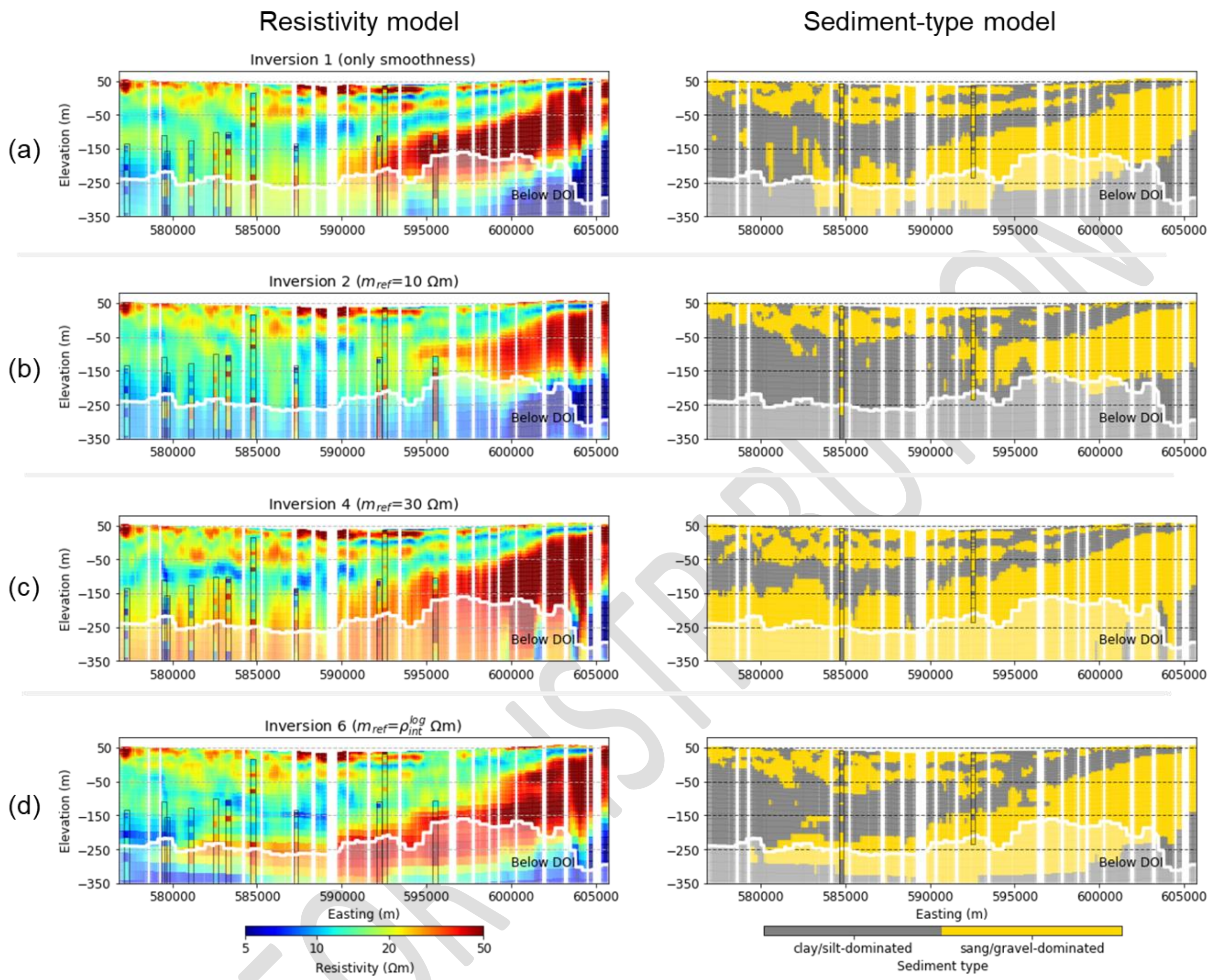

Figure 9. Vertical sections of resistivity and sediment-type models at a flight line: L710601 shown as the red line in Figure 5. The left and right panels distinguish resistivity and sediment-type models. Four recovered resistivity models from Inversion 1, 2, 4, 6 (Table 2) and corresponding sediment-type models derived from them are shown in Figures 9a, 9b, 9c, 9d, respectively. Eleven resistivity logs and two lithology logs within 200 m from this flight line were shown within black rectangles in the left and right panels, respectively. Shaded areas with white transparent color show the region below the depth-of-investigation (DOI).

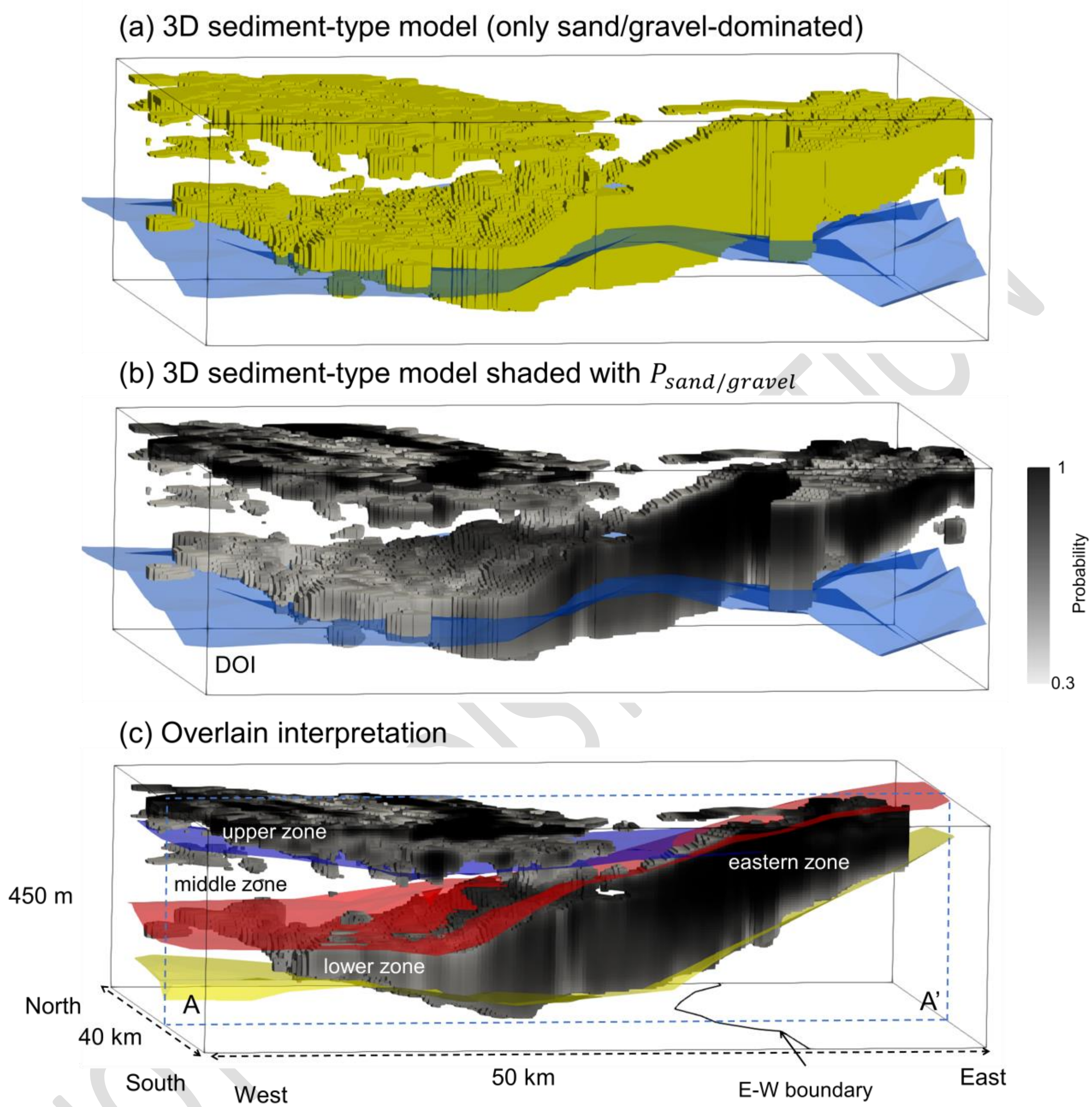

Figure 10. The results of the AEM interpretation workflow in a 3D view. (a) A display of sand/gravel-dominated (yellow color). (b) The regions shown in (a) but shaded with the probability of sand/gravel-dominated, $P_{sand/gravel}$. (c) Overlain interpretation. The model shown in Figure 10c extends from the vertical section A-A' the location of which is shown in Figure 5, and extends to the north. Blue dashed lines indicate the location the A-A' vertical section in the 3D view. The E-W boundary shown as a black line separates the eastern and western part of the regions. In the western part of the region, the upper, middle and lower zones are delineated by the three surfaces – the base of the upper zone (blue), the base of the middle zone (red), the base of the lower zone (yellow). In the eastern part of the region, a single sand/gravel-dominated zone is identified, which is denoted as the eastern zone; the red and blue surfaces in this region correspond to the top and base of the eastern zone.

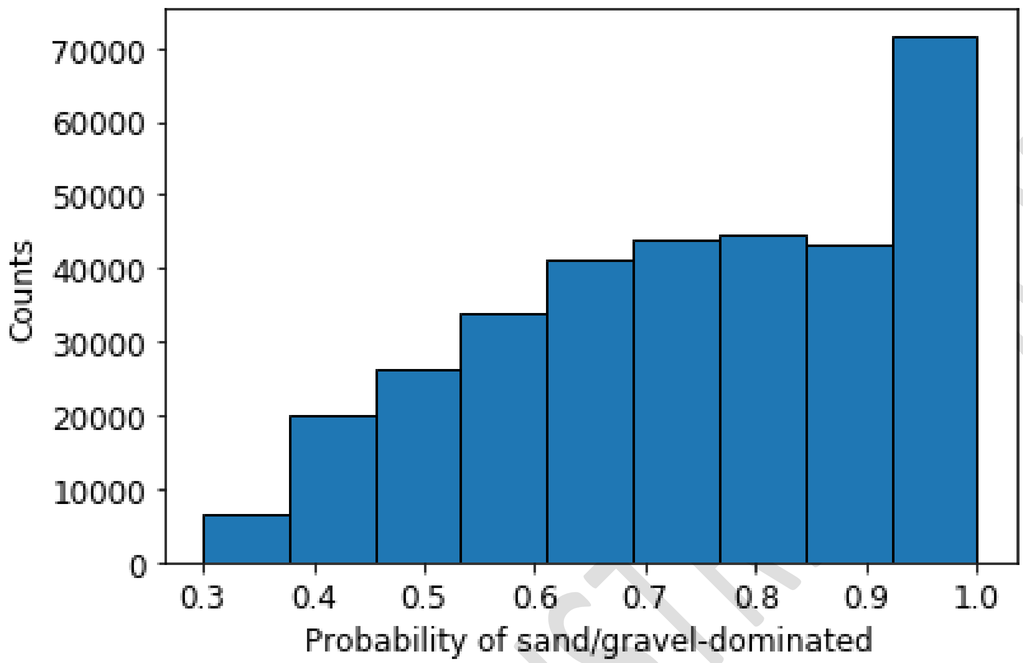

Figure 11. Histogram of the probability of sand/gravel-dominated shown in Figure 10b.

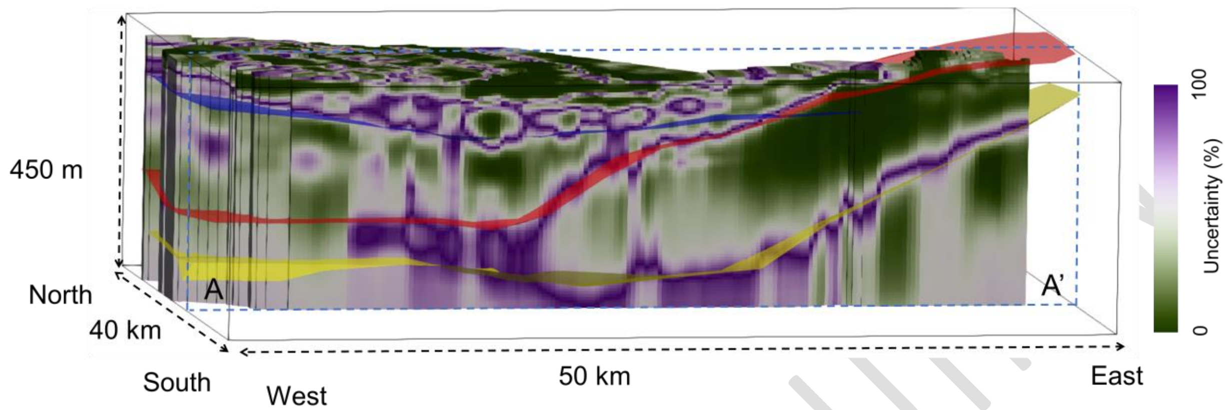

Figure 12. The estimated uncertainty in sediment type from AEM data in a 3D view. The 3D uncertainty extends from the vertical section A-A' the location of which is shown in Figure 5, and extends to the north. Blue dashed lines indicate the location the A-A' vertical section in the 3D view.

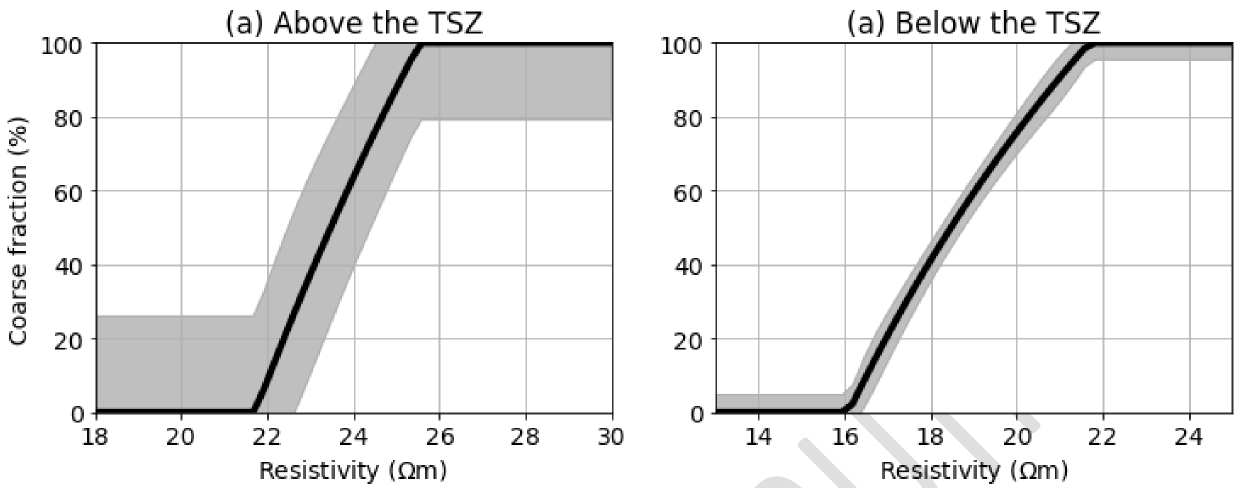

Figure 13. The relationship between resistivity and coarse fraction: (a) above and (b) below the top of the saturated zone (TSZ). Grey shaded region indicates the standard deviation of the coarse fraction illustrating the uncertainty of the transform when converting resistivity values to coarse fraction.

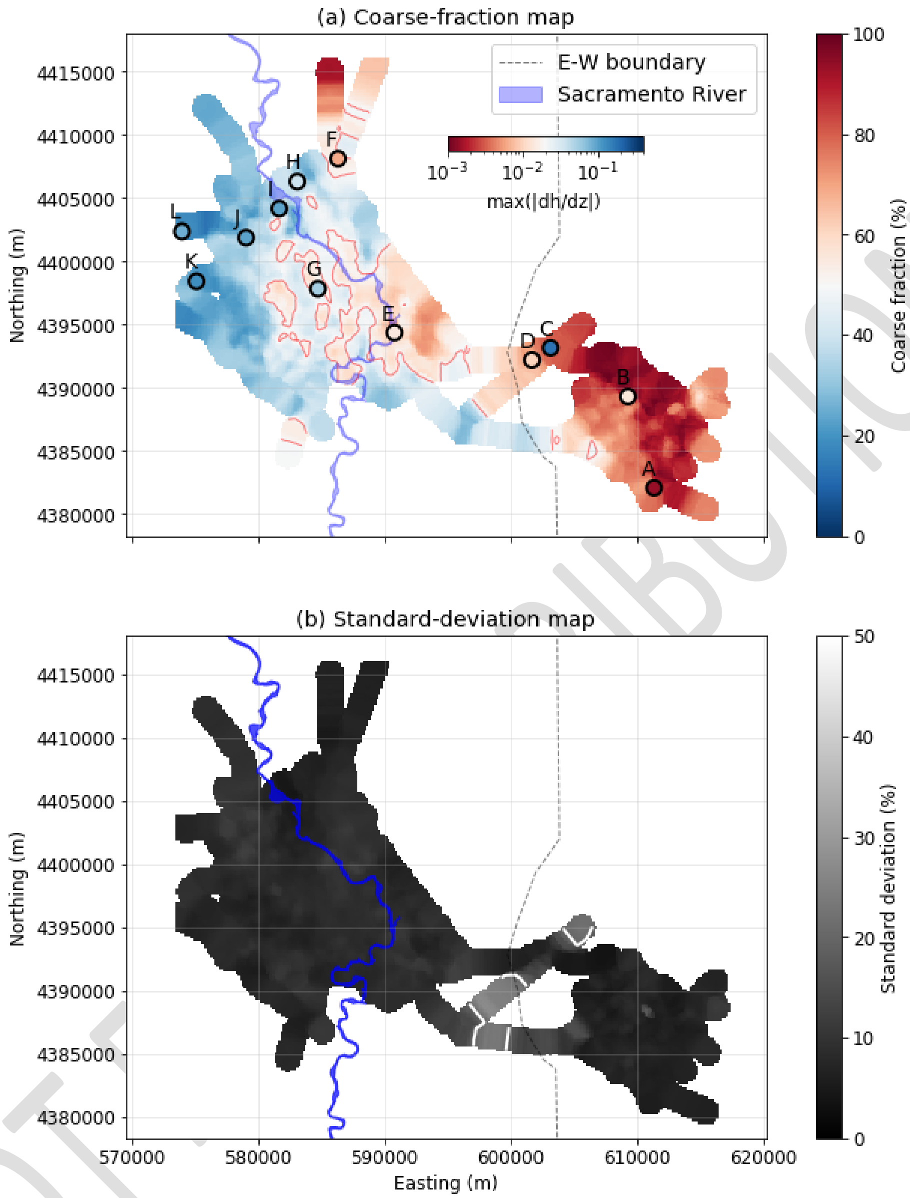

Figure 14. Interpolated maps providing information about the vertical connectivity of the aquifer system and the uncertainty. (a) The coarse-fraction map with location of 12 multi-completion wells indicated by circles color coded with the maximum vertical hydraulic gradient. Letters A–L indicate names of the twelve multi-completion wells. Red contours indicate 50% coarse-fraction values. Black dashed line indicates the E-W boundary delineating the horizontal boundary between the lower and eastern zones. Blue polygon indicates the Sacramento River. (b) The standard-deviation map representing the uncertainty; darker color indicates low uncertainty (i.e., low standard deviation); white contours indicate 10% standard-deviation values.

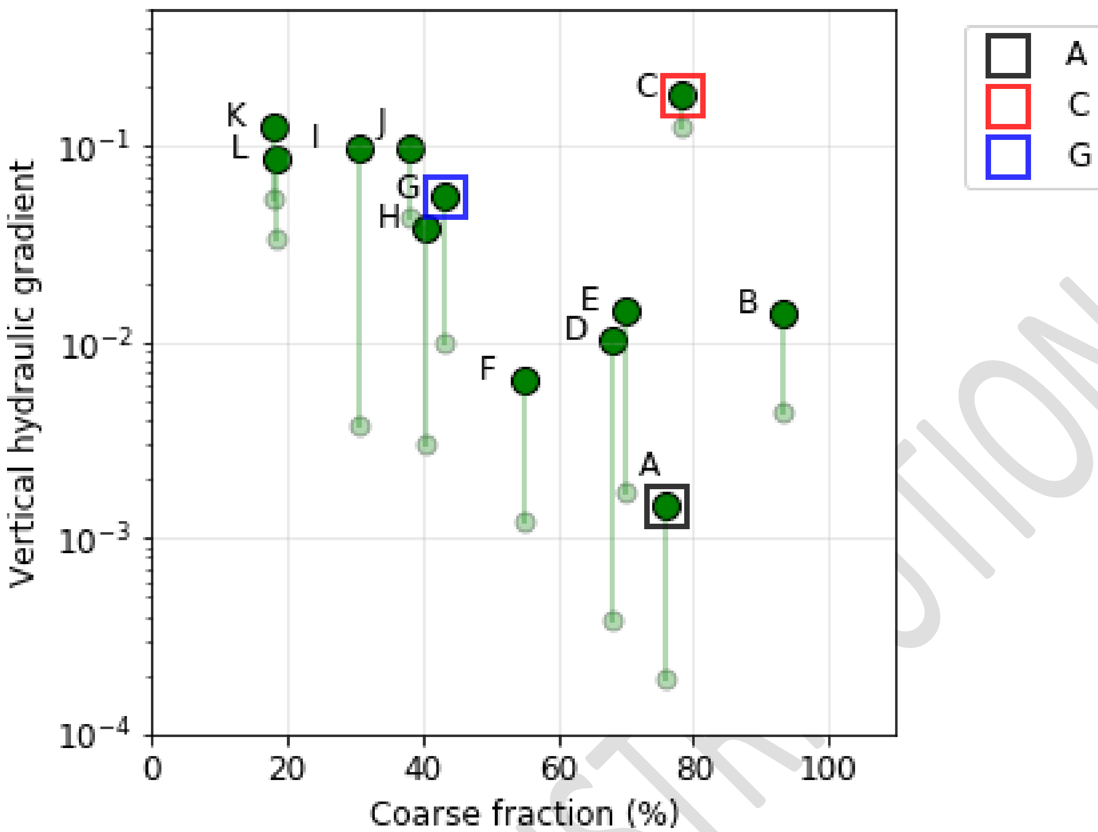

Figure 15. A cross plot of coarse fractions from the AEM data and vertical hydraulic gradients from the head data. Solid and transparent green circles distinguish the maximum and minimum vertical hydraulic gradients, respectively. Letters A-L indicate names of the twelve multi-completion wells, and their locations are shown in Figure 14a. Black, red, and blue rectangles indicate the multi-completion wells labeled as A, C and G, respectively. The hydrographs from the A, G, C wells are presented in Figures 16, 17, 18, respectively.

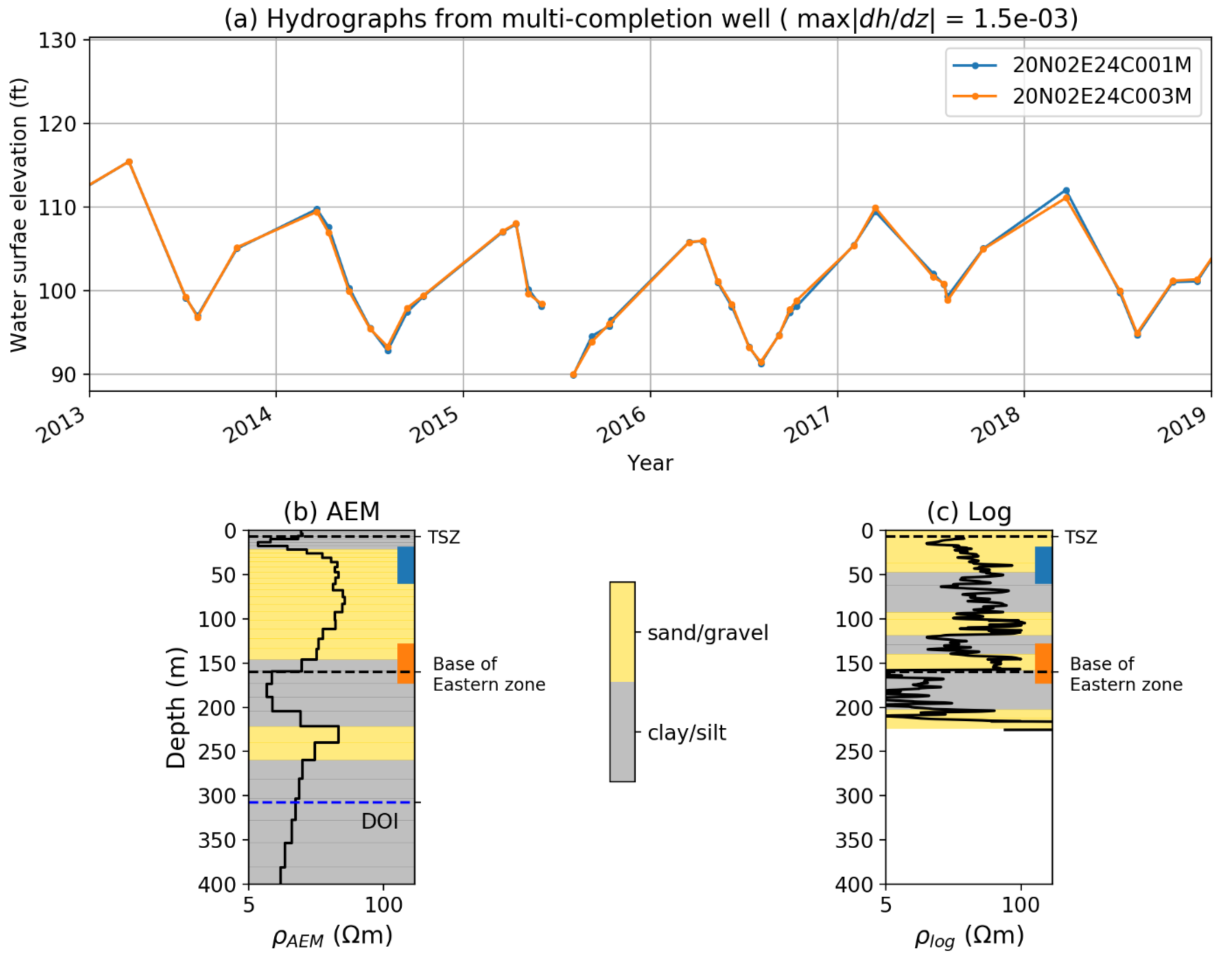

Figure 16. Comparison of the AEM-based information with the head measurements from a multi-completion well (location A in Figures 14a and 15; wellpairID: 20N02E24C). (a) Two hydrographs from the shallower and deeper screen intervals shown as blue and orange curves, respectively; a value of maximum vertical hydraulic gradient is denoted in the title. (b) 1D layered-resistivity and sediment type models from the closest AEM sounding location. (c) Resistivity and lithology logs from a well included in the multi-completion well. The shallower and deeper screened intervals are shown as blue and orange boxes, respectively in Figures 16b and 16c; the TSZ and the base of the eastern zone are shown as black dashed lines in Figures 16b and 16c. The DOI is shown as a blue dashed line in Figure 16b.

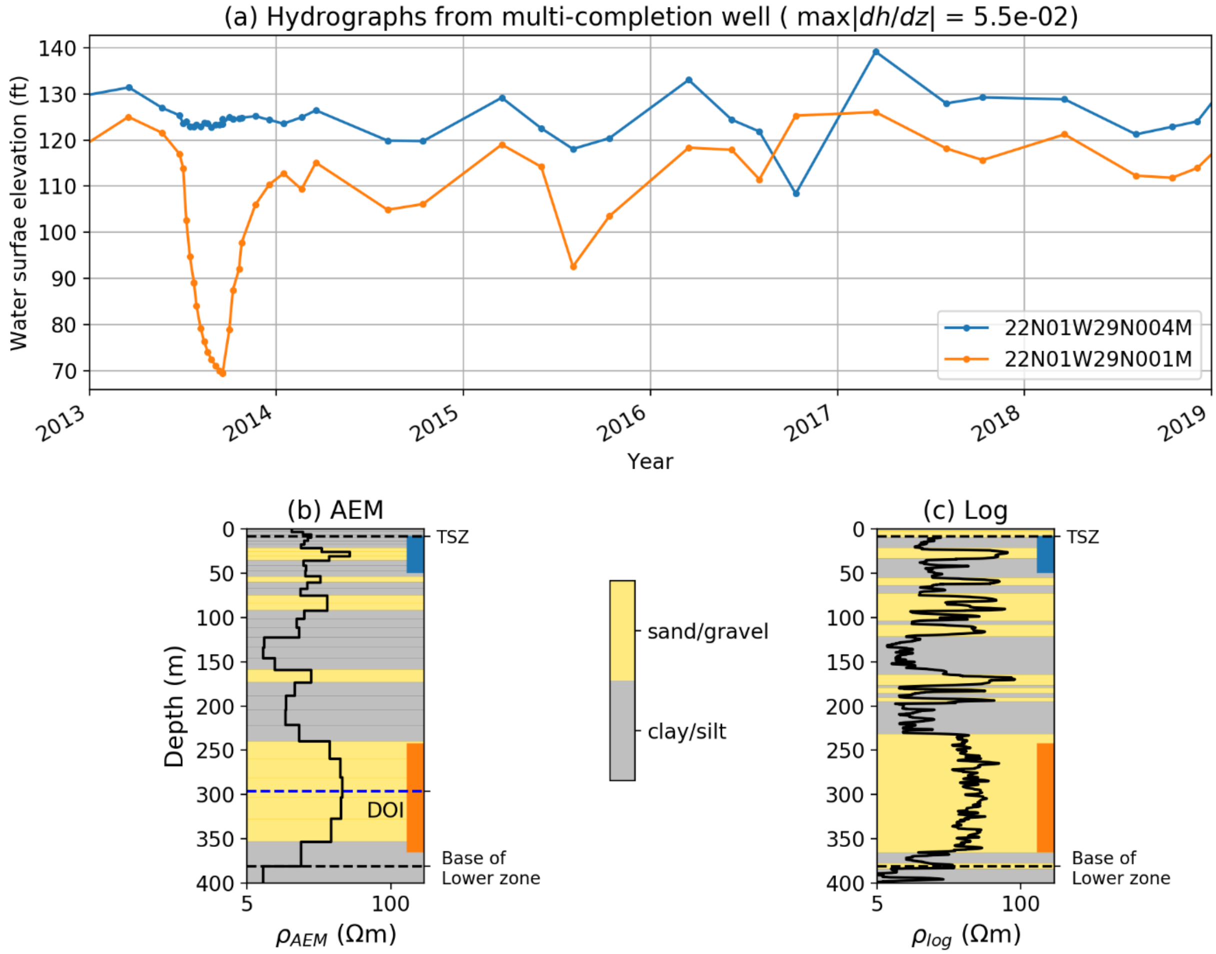

Figure 17. Comparison of the AEM-based information with the head measurements from a multi-completion well (location G in Figures 14a and 15; wellpairID: 22N01W29N). (a) Two hydrographs from the shallower and deeper screen intervals shown as blue and orange curves, respectively; a value of maximum vertical hydraulic gradient is denoted in the title. (b) 1D layered-resistivity and sediment type models from the closest AEM sounding location. (c) Resistivity and lithology logs from a well included in the multi-completion well. The shallower and deeper screened intervals are shown as blue and orange boxes, respectively in Figures 17b and 17c; the TSZ and the base of the lower zone are shown as black dashed lines in Figures 17b and 17c. The DOI is shown as a blue dashed line in Figure 17b.

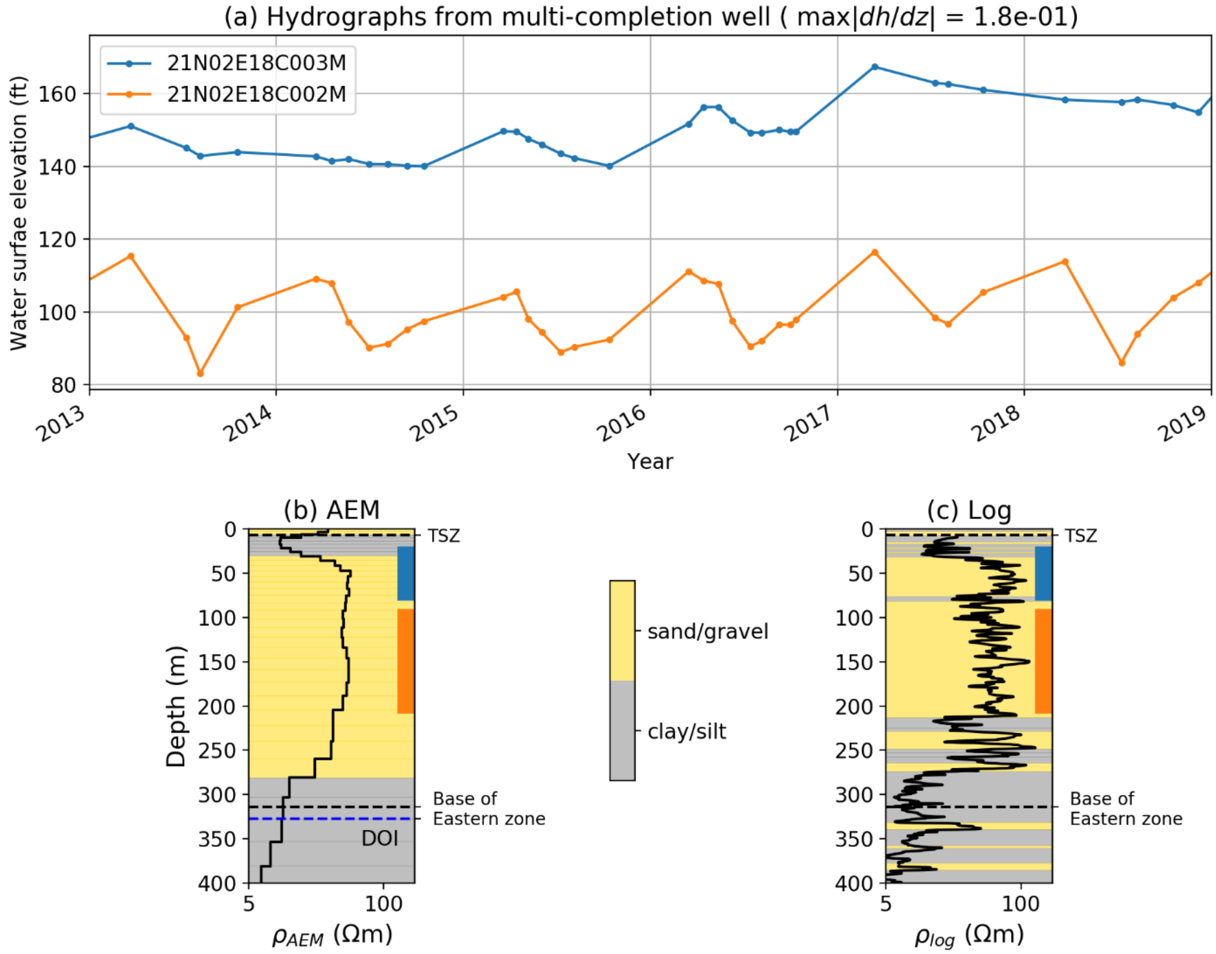

Figure 18. Comparison of the AEM-based information with the head measurements from a multi-completion well (location C in Figures 14a and 15; wellpairID: 21N02E18C). (a) Two hydrographs from the shallower and deeper screen intervals shown as blue and orange curves, respectively; a value of maximum vertical hydraulic gradient is denoted in the title. (b) 1D layered-resistivity and sediment type models from the closest AEM sounding location. (c) Resistivity and lithology logs from a well included in the multi-completion well. The shallower and deeper screened intervals are shown as blue and orange boxes, respectively in Figures 18b and 18c; the TSZ and the base of the eastern zone are shown as black dashed lines in Figures 18b and 18c. The DOI is shown as a blue dashed line in Figure 18b.

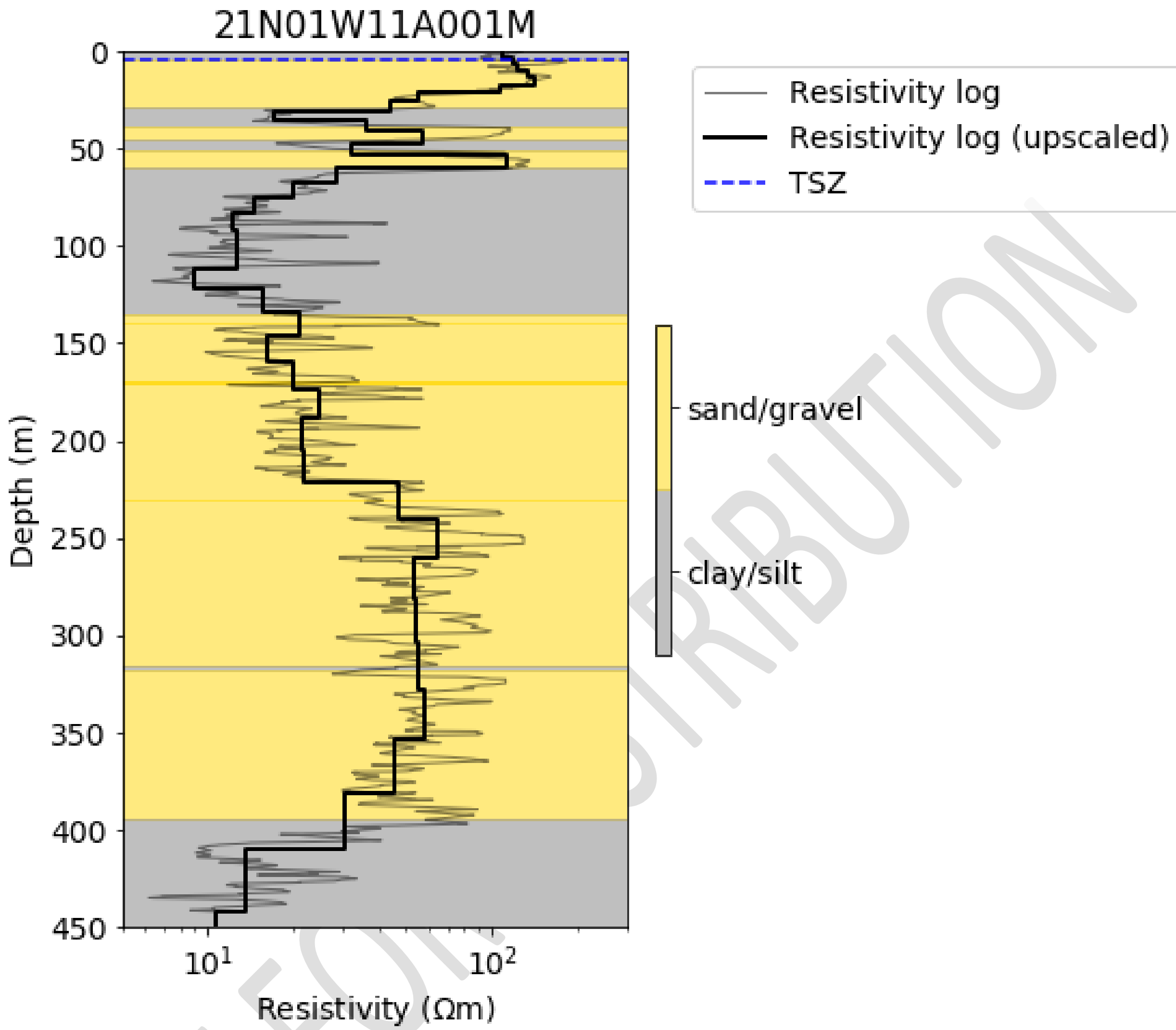

Figure A1. Resistivity and lithology logs at a well location (wellID: 21N01W11A001M). Thin and thick black lines indicate measured resistivity values with half foot sampling rate and upscaled resistivity values into a layering used for the AEM inversion. Grey and yellow shaded layers display lithologic data classified as clay/silt (grey) and sand/gravel (yellow). Blue dashed line indicates the top of the saturation zone (TSZ). The location of the well is denoted as a cross mark in Figure 5.

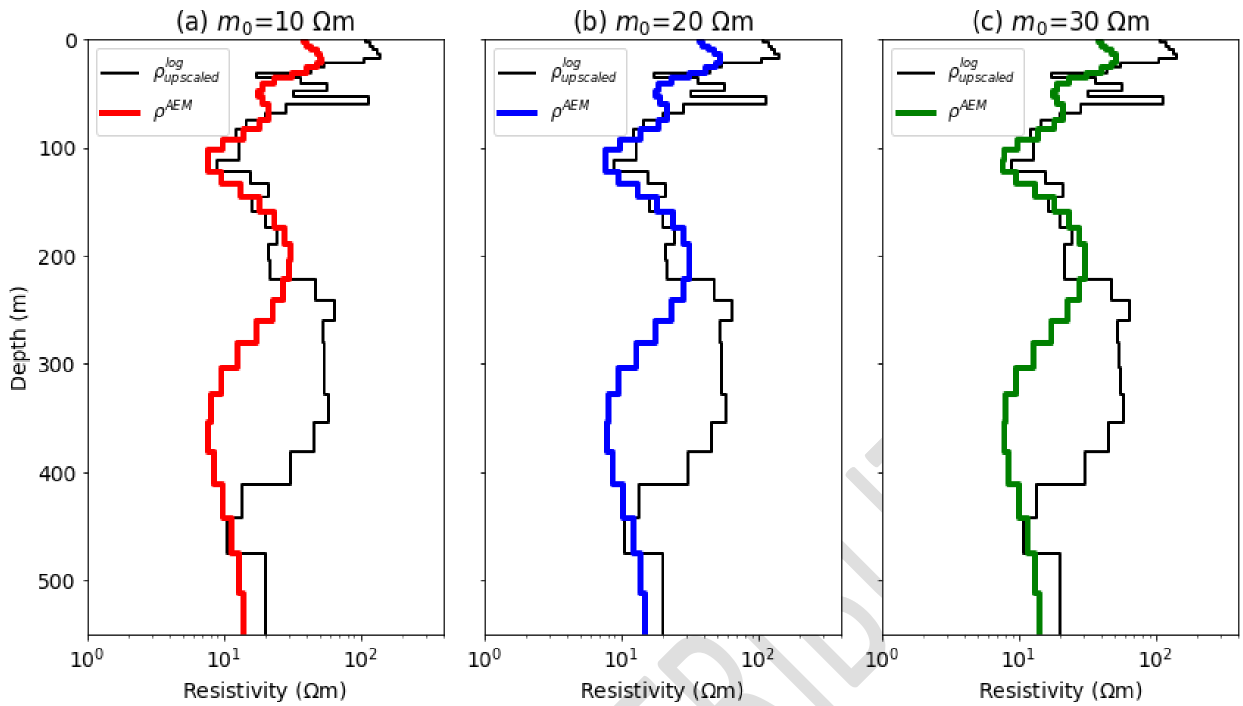

Figure A2. Recovered layered-resistivity models from inversions with variable initial models: (a) 10 Ωm, (b) 20 Ωm, (c) 30 Ωm. Only the smoothness constraint is used for the regularization function.

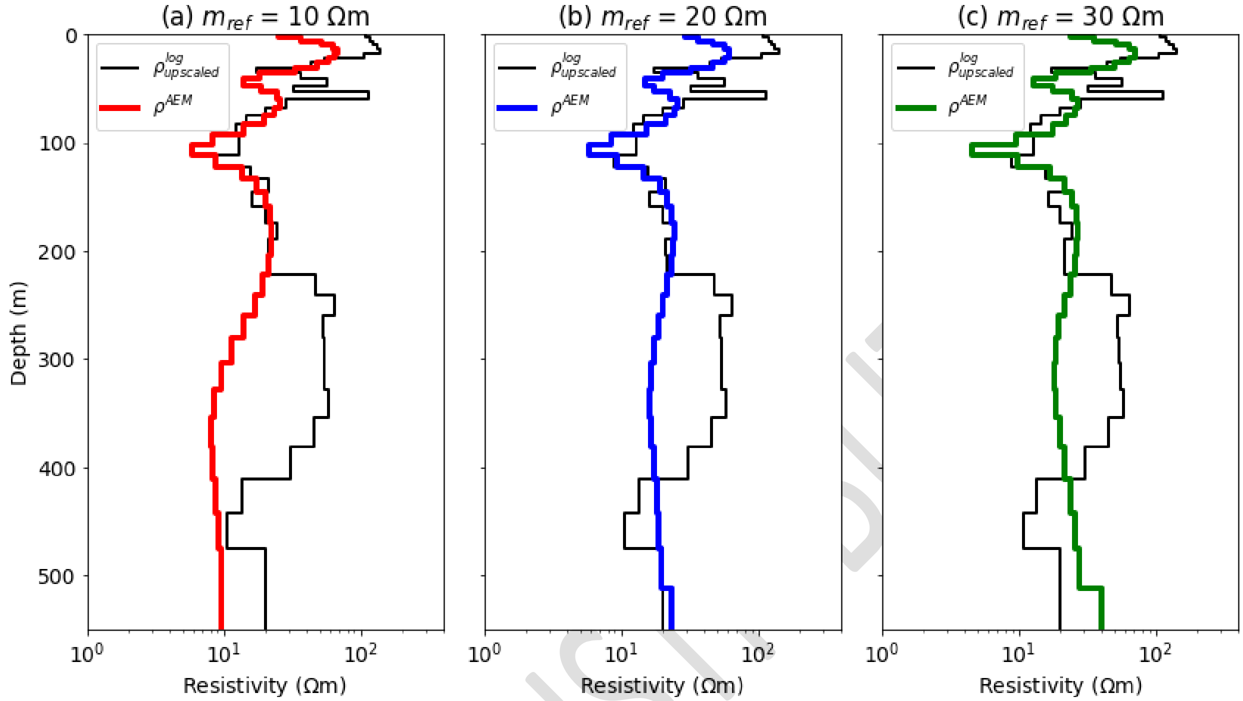

Figure A3. Recovered layered-resistivity models from inversions with homogeneous reference models: (a) 10 Ωm, (b) 20 Ωm, (c) 30 Ωm. Both the smoothness constraint and reference model were used for the regularization function.

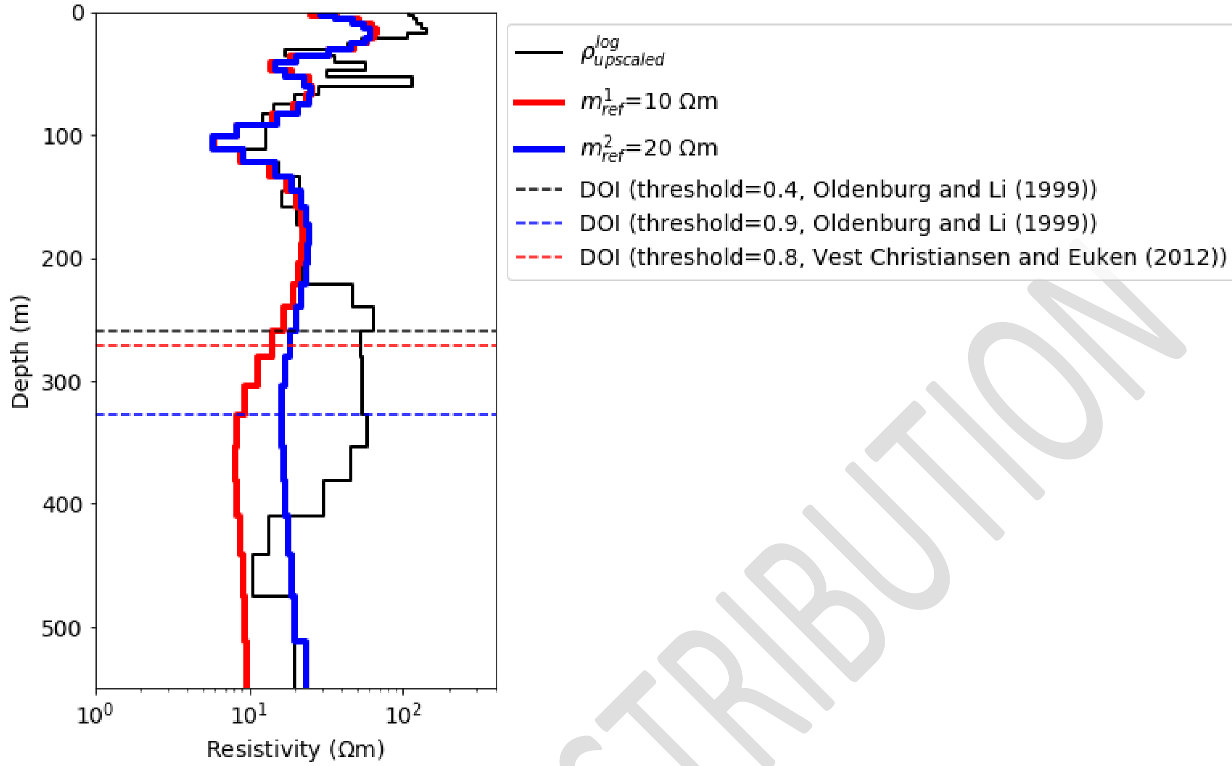

Figure A4. Estimating depth of investigation (DOI) using Oldenburg & Li (1999)'s approach. The two layered-resistivity models recovered from inversions with different reference models: 10 Ωm and 20 Ωm are distinguished as red and blue lines. Estimated DOI values with threshold values of 0.4 and 0.9 are shown as black and blue dashed lines, respectively. For comparison an estimated DOI value from Vest Christiansen & Auken (2012)'s approach with a threshold value of 0.8 is shown as red dashed line. Black line shows the upscaled resistivity log.

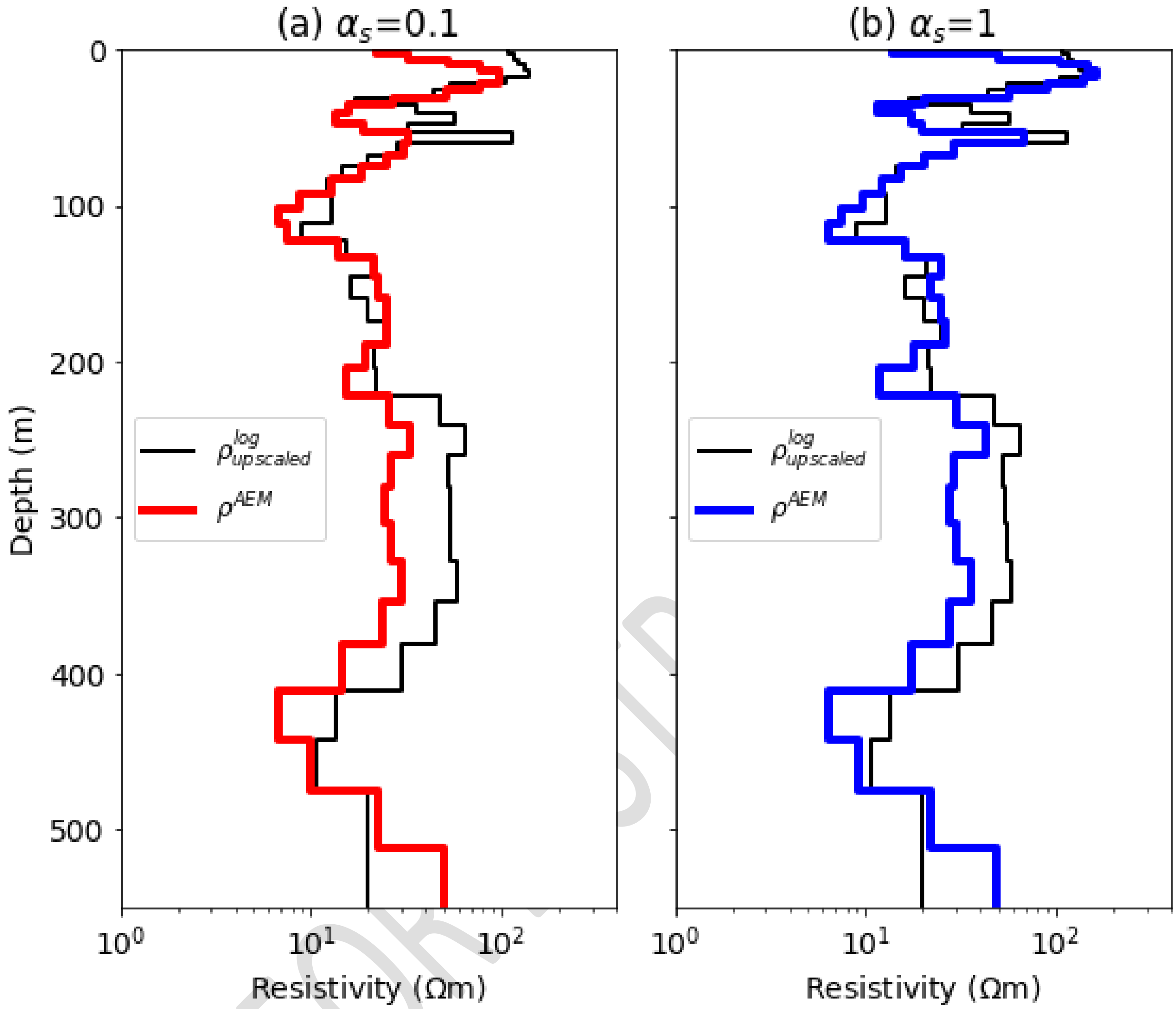

Figure A5. Recovered layered-resistivity models from inversions by using the upscaled resistivity log as a reference model with variable α_s values: (a) 0.1 and (b) 1. Black line shows the upscaled resistivity log. Both the smoothness constraint and reference model were used for the regularization function.

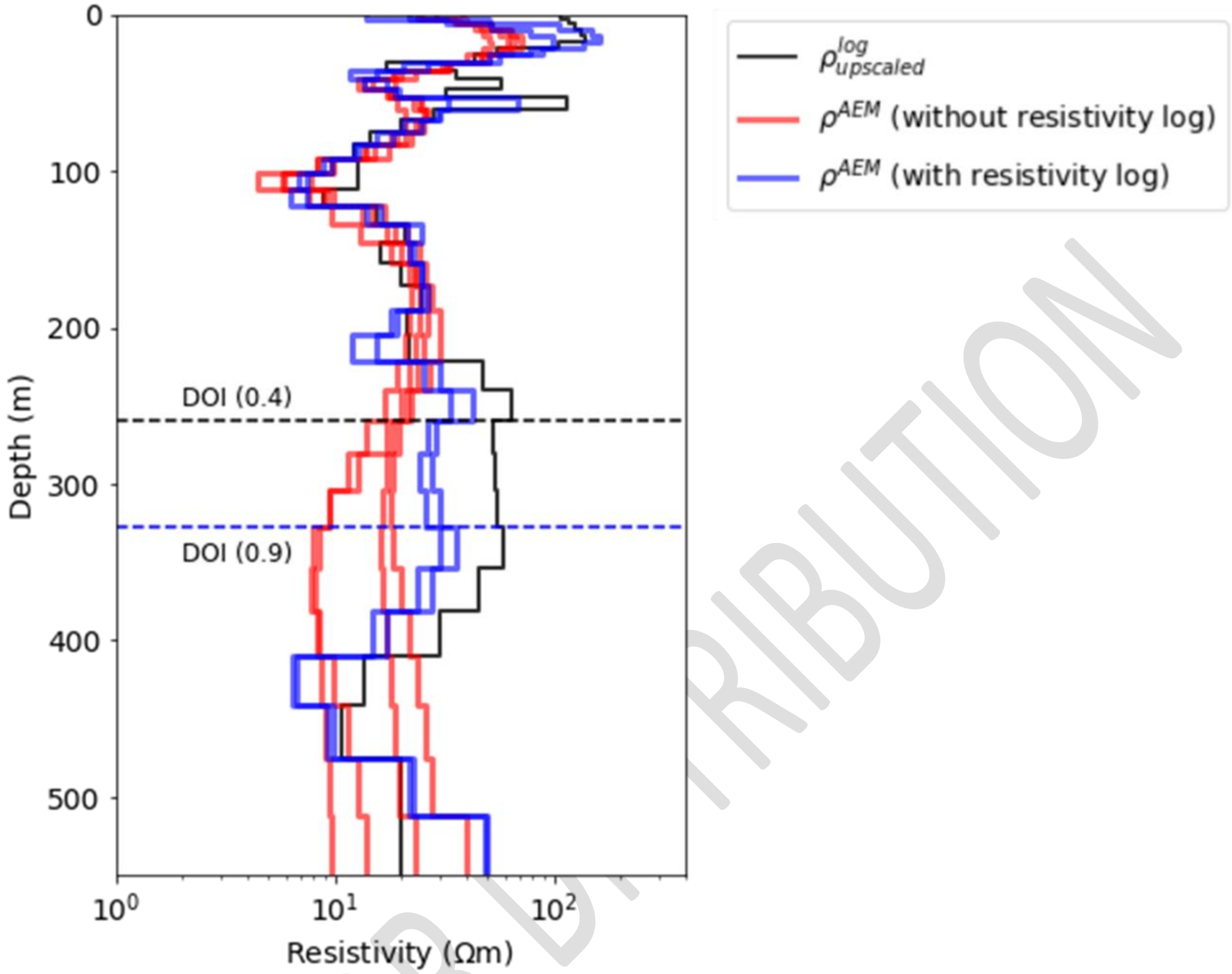

Figure A6. Six layered-resistivity models recovered from 1D AEM inversions with different prior models. Red and blue lines distinguish whether the upscaled resistivity log was used as a reference model or not. Black line shows the upscaled resistivity log. Black and blue dashed lines show the DOIs with threshold values of 0.4 and 0.9, respectively.

Table 1. Specifications of the dual moment SkyTEM 312 and 304 systems. The dual moment system includes the low moment (LM) and high moment (HM).

	SkyTEM 312		SkyTEM 304	
	LM	HM	LM	HM
Transmitter area (m^2)	342	342	342	343
Base frequency (Hz)	30	210	30	210
Pulse width (ms)	0.8	4	0.8	4
Ramp-off time (μs)	15	310	5	41
Time range (from the peak input current)	26 μs–1.4 ms	376 μs–10.7 ms	26 μs–1.4 ms	86 μs–10.4 ms
Peak current (A)	6	110	9	111
Number of coil turns (for transmitter)	2	12	1	4

Table 2. Six different sets of inversion parameters. Explanation of inversion parameters are described in section 4.1.2. For inversion numbers 5 and 6, we generated an interpolated resistivity model using 152 resistivity logs, ρ_{int}^{log}, and this was used as a reference model. The inverse distance weight, w_{IDW}, used for the interpolation was used as a cell-based weighting for the smallness term, w_s, to compensate AEM soundings far way from the resistivity logs.

Inversion number	m_0	m_{ref}	α_s	α_z	α_r	w_s
1	10 Ωm	N/A	N/A	1	5	1
2	10 Ωm	10 Ωm	1	1	5	1
3	10 Ωm	20 Ωm	1	1	5	1
4	10 Ωm	30 Ωm	1	1	5	1
5	10 Ωm	ρ_{int}^{log}	0.1	1	5	w_{IDW}
6	10 Ωm	ρ_{int}^{log}	1	1	5	w_{IDW}